Spaceborne thermal infrared observations of Arctic sea ice leads at 30 m resolution

Yujia Qiu[1, 2, 3], Xiao-Ming Li[2, 1], Huadong Guo[2, 1]

[1]Key Laboratory of Digital Earth Science, Aerospace Information Research Institute, Chinese Academy of Sciences, Beijing 100094, China
[2]International Research Center of Big Data for Sustainable Development Goals, Beijing 100094, China
[3]University of Chinese Academy of Sciences, Beijing 100049, China

Correspondence to: Xiao-Ming Li (lixm@radi.ac.cn)

Abstract. Sea ice leads ~~are elongated fractures within sea ice cover,~~ play~~ing~~ an important role in the heat exchange ~~from~~ between the ocean ~~to~~and the overlying atmosphere, particularly narrow leads with widths of less than 100 meters.~~.~~ We present a method for detecting sea ice leads in the Arctic using high-resolution infrared images from the Thermal Infrared Spectrometer (TIS) on board the Sustainable Development Science Satellite 1 (SDGSAT-1), with a resolution of 30 m in a swath of 300 km. With the spatial resolution of leads observed by infrared remote sensing increasing to tens of meters, focused on the Beaufort Sea cases in April 2022, we achieved an overall accuracy of 96.3% in lead detection compared to the Sentinel-2 visible images. For the three infrared bands of the TIS, the B2 (10.3-11.3 µm) and B3 (11.5-12.5 µm) bands, show similar performances in detecting leads. The B1 band (8.0-10.5 µm) can be usefully complementary to the other two bands, as a result of different temperature measurement sensitivity. Combining the detected results from TIS three bands, the TIS is able to detect more leads with widths less than hundreds of meters compared to the Moderate-Resolution Imaging Spectroradiometer (MODIS). Our results demonstrate that SDGSAT-1 TIS data at 30 m resolution can effectively observe previously unresolvable sea ice leads, providing new insight into the contribution of narrow leads to rapid sea ice changes in the Arctic.~~Narrow leads less than a hundred meters in width contribute considerable heat fluxes, requiring fine-scale observation of Arctic leads. With the launch of Sustainable Development Science Satellite 1 (SDGSAT-1) by China on 5 November 2021, the on-board Thermal Infrared Spectrometer (TIS) provides thermal infrared imagery at an unprecedented resolution of 30 m in a swath of 300 km. We propose a method adapted to the TIS high-resolution infrared images for lead detection in the Arctic. For the first time, the spatial resolution of leads by infrared remote sensing increases from the scale of~~ hundreds ~~kilometers to tens of meters. For the Beaufort Sea cases in April 2022, the detection is consistent with the Sentinel-2 visible images, yielding an overall accuracy of 96.30%. Compared with the Moderate-Resolution Imaging Spectroradiometer (MODIS), the TIS presents more leads with width less hundreds of meters than the results based on the MODIS data. For the three infrared bands of the TIS, the B2 (10.3-11.3 µm) and B3 (11.5-12.5 µm) bands, show similar performances in detecting leads. The B1 band (8.0-10.5 µm) can be complementary to the other two bands, as the temperature measurement sensitivity is different from the other two, benefiting better detection by combining the three bands. This study demonstrates that SDGSAT-1 TIS data at 30 m resolution is well applicable for observing previously~~

~~unresolvable~~ sea ~~ice leads, and will provide insight into the contribution of narrow leads to rapid sea ice changes in the Arctic.~~

1 Introduction

Over several decades, the Arctic has experienced ~~has~~ warm~~ed~~ing at approximately twice the rate as the ~~entire~~ globe average, ~~as the result of~~ a ~~well-known~~ phenomenon known ~~of~~as Arctic amplification (Serreze and Francis~~Arrhenius~~, ~~1896~~2006) that has attracted increasing attention. Among a suite of causes and processes contributing to Arctic amplification~~Arctic amplification causes and processes~~, ~~the~~ ongoing changes in the Arctic sea ice extent and the heat fluxes between the ocean and ~~the~~ atmosphere are particularly prominent (Serreze and Barry, 2011). Leads are elongated fractures within sea ice~~ cover, which~~ that develop as ~~the~~ a result of sea ice fracturing under wind and ocean stresses. Although these ~~area of these~~ openings ~~is~~are relatively small, covering less than 2% of the central Arctic, ~~leads~~they hold significant importance for the Arctic mass and heat balance (Vihma et al., 2014). Open water in leads may refreeze when exposed to ~~a~~ cold atmosphere, leaving ~~so leads contain~~ unfrozen water and ice of varying thicknesses. ~~Although the area of these openings is relatively small, covering less than 2% of the central Arctic, leads hold significant importance for the Arctic mass and heat balance (Vihma et al., 2014).~~ A small change of 1% in the lead fraction ~~would~~ can cause a large fluctuation in ~~the~~ air temperature, ~~by~~ up to 3.5 K (Lüpkes et al., 2008). Leads provide windows for heat exchange between the air and water, contributing to ~~more than~~over 70% of ~~the~~ upward heat flux (Marcq and Weiss, 2012). During winter, newly opened leads and polynyas are the primary ~~main~~ source of ice production, brine rejection, and turbulent heat loss to the atmosphere (Maykut, 1982; Alam and Curry, 1998). In spring, surface melt creates more openings, ~~and releases~~ allowings more heat exchange ~~into~~ with the atmosphere (Ledley, 1988; Tschudi et al., 2002). As preferential melting sites in early summer (Alvarez, 2022), leads strongly absorb shortwave radiation during the melting season, promoting lateral and basal melt of sea ice (Maykut, 1982), accelerating sea ice thinning (Kwok, 2018) and decreasing the mechanical strength of sea ice (Gimbert et al., 2012); these processes enable a more considerable drifting speed, deformation, and possibly a faster export (Rampal et al., 2009; Onarheim et al., 2018). In turn, more fracturing and earlier openings are expected to create more intensive networks of leads in the following spring (Steele et al., 2015).

Under the ongoing trend of sea ice retreat in the Arctic (Cavalieri and Parkinson, 2012; Stroeve et al., 2012), identifying the characteristics of sea ice leads can help enhance our understanding of thermodynamic and mechanical processes in the Arctic. Since the early 1990s, ~~V~~various remote sensing instruments, especially by moderate-resolution thermal infrared satellite images, –have been used for sea ice lead research~~ since the early 1990s~~, ~~especially by moderate-resolution thermal infrared satellite images,~~ e.g., the Advanced Very High-Resolution Radiometer (AVHRR) (Key et al., 1993; Lindsay and Rothrock, 1995), Moderate-Resolution Imaging Spectroradiometer (MODIS) (Willmes and Heinemann, 2015a and 2015b; Hoffman et al., 2019 and 2021; Reiser et al., 2020; Qu et al., 2021), ~~and~~ Landsat-8 Thermal Infrared Sensor (TIRS) (Qu et al., 2019; Fan et al., 2020) ~~data~~and FY-D Moderate Resolution Spectral Imager Type II (MERSI-II) (Wang et al., 2022). High--resolution optical data ~~is~~has also been used for lead detection (Marcq and Weiss, 2012; Muchow et al., 2021). Other studies have ~~also~~ applied active and passive microwave data to lead detection, taking ~~with the~~ advantage ~~that~~ of the transparency of microwave wavelengths ~~are transparent~~ to cloud cover; however, ~~either~~ the data resolution in these studies is either too coarse, e.g., ~~with~~ the Advanced Microwave Scanning Radiometer for Earth Observing System (AMSR-E) with a resolution of 6.25 km (Röhrs and Kaleschke, 2012; Bröhan and Kaleschke, 2014) or the observations are discontinuous, e.g., by synthetic aperture radar (SAR) (Murashkin and Spreen, 2018; Murashkin et al., ~~and~~ 2019~~9~~; Liang et al., 2022) and altimeter (Wernecke and Kaleschke, 2015; Lee et al., 2018; Zhong et al., 2023). Table 1~~Table 1~~ summarizes the ~~current~~ publicly available lead datasets, mainly developed ~~from~~ based on moderate resolution thermal infrared, with spatial resolutions on a ~~kilometre~~kilometer scale, limited to the winter season.

The key to detecting sea ice leads using thermal infrared data ~~For sea ice lead detection based on thermal infrared data, the key~~ lies in deriving thermal contrasts, specifically ~~namely,~~ the temperature anomaly between sea ice and open water, and ~~to~~ distinguishing leads from thermal contrasts of ice ages and clouds. To this end, previous studies have utilized various temperature datasets~~various temperature datasets were used in previous studies~~. For instance, Willmes and Heinemann (2015a) ~~utilized~~ used the MODIS ice surface temperature (IST) product to map pan-Arctic lead distribution from January to April over the period of 2003 to 2015. They also developed ~~The~~a long-term daily lead product~~ is available~~ to assess seasonal divergence patterns of sea ice in the Arctic Ocean (Willmes and Heinemann, 2015b). Essentially, IST data, which are usually ~~generally~~ retrieved ~~by~~ using the split-window technique (Key et al., 1997), are less accurate ~~under~~ in the presence of melt ponds and leads because of the lower emissivity (0.96 compared to 0.99) of water compared to~~than~~ sea ice~~, because the lower emissivity (0.96 compared to 0.99) can~~ causing~~e~~ a difference in the retrieved temperature (Hall et al., 2001). Moreover~~Furthermore~~, cloud masking defects affect lead detection (Hoffman et al., 2019; Reiser et al., 2020). To address these limitations, Hoffman et al. (2019) focused on using at-sensor brightness temperature (BT) data and improved cloud masking to detect leads ~~. They detected leads~~ for January through April over the period of 2003 to 2018.~~,~~ However, the lead area estimation was lower than that of~~presenting a lower estimation for the lead area compared with the results in~~ Willmes and Heinemann (2015~~c~~b)~~; the reason is~~ due to ~~the~~ differences in the spatial resolutions of the lead datasets (1 km^2 compared to 2 km^2, ~~see~~as listed in Table 1~~Table 1~~). More recently,~~The recently~~ Hoffman et al. (2021) ~~published work~~ applied ~~the~~ a convolutional neural network U-Net to detect leads based on Visible Infrared Imaging Radiometer Suite (VIIRS) 11 µm BT images~~ for lead detection~~ (Hoffman et al., 2021). The lead area analysis ~~of lead area~~ over the winter season ~~from~~ between 2002 to 2022 showed ~~had~~ a ~~small~~ slight decreasing trend due to increasing cloud cover in the Arctic, but an increasing trend of 3,700 km^2 per year after removing the impact of cloud cover changes (Hoffman et al., 2022a). Qu et al. (2021) proposed a modified algorithm from Willmes and Heinemann (2015a) to detect daily spring leads in the Beaufort Sea based on the IST data retrieved from MODIS swath products, providing better results in ~~terms of~~ identifying open water leads and refrozen leads; they found a positive interannual trend in the April lead area for the study period of 2001 to 2020 of approximately 2,612 km^2 per year.

Accurate ~~Adequate~~ lead observations are crucial to ~~have important contributions to~~ understanding rapid sea ice changes in the Arctic Ocean (Zhang et al., 2018; Ólason et al., 2021). Narrow leads of less than a hundred meters in width are over two times more efficient at transmitting turbulent heat than larger leads of hundreds of meters (Marcq and Weiss, 2012). However, due to the limitations of spaceborne thermal infrared sensors in terms of spatial resolution, current lead observations are only available ~~only up to~~at a moderate resolution on a kilometer scale. Key et al. (1994) assessed the effect of sensor resolution on lead width statistics~~. They~~ and suggested that the mean lead width expands ~~“grows”~~ as the pixel size builds up in gradually degraded images~~The narrowest lead widths that can be revealed by the detection are several kilometers or even coarser (Key et al., 1993)~~. Qu et al. (2019) resampled Landsat-8 TIRS data with a resolution of 100 m to 30 m to estimate heat fluxes over the detected leads. Their result showed an underestimated lead information detected by MODIS data compared to TIRS data~~, owing to the inability of MODIS to resolve small leads (widths smaller than 1 km)~~. Consequently, the heat flux estimation from Landsat-8 TIRS data is larger than that from MODIS data, where small leads contribute to more than a quarter of the total heat flux. Yin et al. (2021) proposed a convolutional neural network-based framework to estimate turbulent heat flux over leads at the sub-pixel scale, using~~based on~~ MODIS data. The super-resolution estimates are better than those obtained ~~estimated by~~from the original moderate resolution data (1 km) and ~~by~~ interpolation-based ~~high~~ high-resolution data (100 m), but still have limitations for very narrow leads. Consequently, ~~Therefore,~~ the kilometer-scale spatial resolution is inadequate for reproducing the actual lead characteristics in the Arctic Ocean. ~~on a kilometer-scale does not support the reproductionparameterization of actual lead characteristics in the Arctic Ocean.~~ High-resolution observations are essential ~~urgently needed to~~for revealing narrow leads and their ~~variability processes~~dynamics.

An emerging opportunity to obtain high-resolution observations is the Sustainable Development Science Satellite 1 (SDGSAT-1), which was successfully launched on November 5, 2021, and is the first satellite customized for the United Nations (UN) 2030 Agenda for Sustainable Development (Guo et al., 2022). Three payloads, the thermal infrared spectrometer (TIS), Glimmer Imager for Urbanization (GIU), and Multispectral Imager for Inshore (MII), allow the satellite to obtain high-quality data as well as full-time monitoring capabilities to facilitate the evaluation of SDG indicators (Guo, 2019; Guo et al., ~~2022~~2021). The TIS is used for global thermal radiation detection with three thermal infrared bands (~~see Table 1~~see Sect~~ion~~. 2.1 for data details~~for the sensor characteristics~~). More importantly, the TIS has a spatial resolution of 30 m, ~~parallel~~ with a wide swath of 300 km. With such an unprecedented infrared imaging capability, SDGSAT-1 TIS is expected to provide far more details of sea ice characteristics in polar regions than current thermal infrared sensors in orbit. To date, the TIS has acquired substantial high-resolution thermal infrared data from the critical seas in the Arctic, ~~e.g.,~~including the Beaufort Sea and the Laptev Sea. Figure 1 presents a few cases in March and April 2022 under clear sky conditions. Under such attractive prospects, we pioneered the scientific application ~~based on~~of SDGSAT-1 TIS data to examine its feasibility in detecting sea ice leads from the Arctic Ocean. With regard to the thermal characteristics of high-resolution data, we proposed an improved lead detection method based on a combination of ~~a~~ binary segmentation and ~~a~~ designed filter. To determine the reliability of the detailed features resolved at 30 m resolution, a series of comparisons were performed, including comparisons with visible and SAR data at high resolutions, as well as comparisons with comparable ~~sea ice~~ lead products at moderate resolutions.

This study focuses on observing Arctic sea ice leads based on spaceborne thermal infrared remote sensing at 30 m resolution and reveals more details than the moderate-resolution thermal infrared sensors~~This study focuses on observing Arctic sea ice leads based on spaceborne thermal infrared remote sensing at 30 m resolution~~~~This study is the first to observe Arctic sea ice leads at 30 m resolution and reveals the details that are unresolvable by moderate-resolution thermal infrared sensors~~. The results will help to understand the processes of Arctic lead variability and its contribution to Arctic sea ice retreat. The paper is organized as follows. Section 2 introduces the data used in this study, including SDGSAT-1 TIS data for lead detection, visible images for validation, and others for comparative analysis. Section 3 presents the method applied to derive sea ice leads. Section 4 presents the high-resolution lead detection results of this study, the validation against visible images, the cross-comparison among three infrared bands, and the comparison with moderate-resolution results. In ~~Section~~ Sect. 5, we explore the factors affecting lead detection and the lead properties resolved by high-resolution imagery. Finally, a summary and conclusion are given in ~~Section~~ Sect. 6.

Table 1. Arctic sea ice lead ~~datasets~~products ~~and~~ with their spatial resolutions and time spans

Dataset	Satellite sensor	Spatial resolution	Time span and seasonal coverage	
Röhrs~~Bröhan~~ and Kaleschke~~Kaleschke~~ (20142)	AMSR-E	6.25 km × 6.25 km	2002 to 2011	November to April
Willmes and Heinemann (2015b)	MODIS	2 km^2	2003 to 2015	January to April
Reiser et al. (2020)	MODIS	1 km^2	2002 to 2021	November to April
Hoffman et al. (2021)	MODIS	1 km^2	2002 to 2022	November to April
	VIIRS	1 km^2	2011 to 2022	November to April

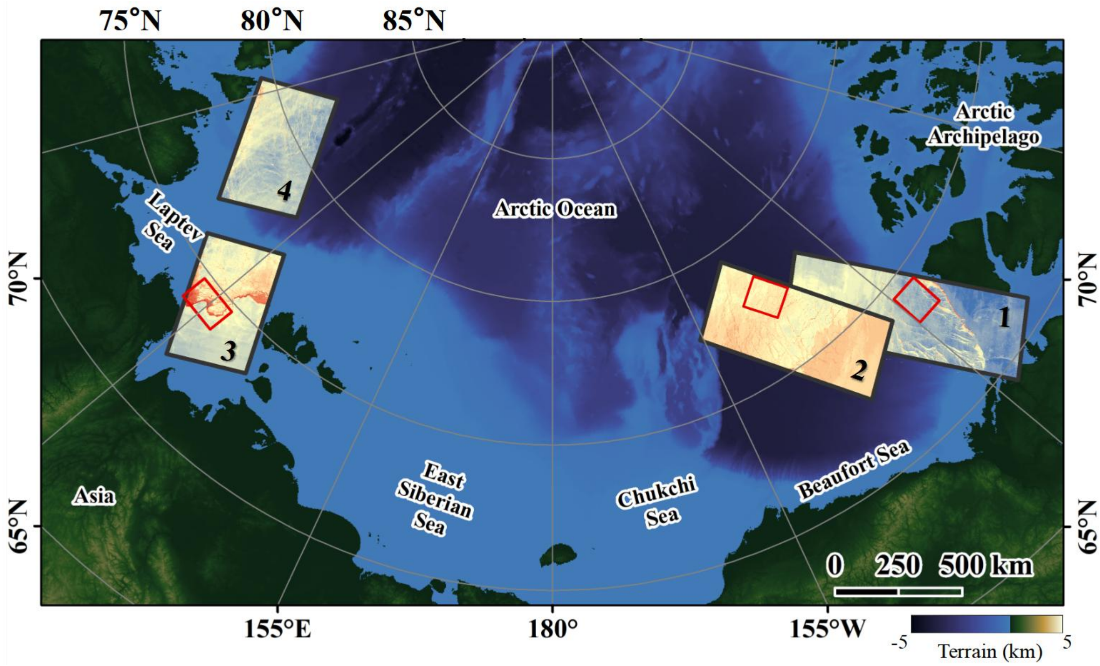

Figure 1: Geospatial distributions of SDGSAT-1 TIS data collected from the Arctic Ocean in March and April in 2022 used in this study for sea ice lead detection. The black borders mark four successive groups of cloudless images (group 1 was acquired on 3 April, group 2 on 28 April, groups 3 and 4 on 23 March), ~~where~~ with ~~the~~ color representsing the BT values from the TIS B2 band. The small red squares indicate ~~are the~~ regions where the TIS data are matched with ~~the~~ Sentinel-2 visible images for validation.

2 Data and pre-processing~~Data~~

2.1 SDGSAT-1 TIS

As listed in Table 2, the TIS has three infrared bands, which are centered at 9.3 μm (8.0-10.5 μm, Band 1 (B1)), 10.8 μm (10.3-11.3 μm, Band 2 (B2)), and 11.8 μm (11.5-12.5 μm, Band 3 (B3)) and has the ability to resolve temperature differences as low as 0.2°C (@ 300 K) (Guo et al., 2022). In the commissioning phase of the satellite, the analysis shows that the accuracy of the radiometric measurement is better than 0.42 K for the three bands (Hu et al., 2022), ~~which~~ satisfying~~ies~~ the preflight requirements (≤1 K). In particular, t~~T~~he B1 band shows less strip noise (i.e., signal fluctuations along the sensor scan caused by detector noise) than the other two bands. The B2 and B3 bands are ~~the two split-window channels~~ widely used in surface temperature retrieval as two split-window channels, while the B1 band is not commonly used in infrared observation missions. Liu et al. (2021) estimated the ability of SDGSAT-1 TIS data to retrieve land surface temperature when different split-window algorithms were applied, i.e., the generalized split-window algorithm using the B2 and B3 bands and the three split-window algorithm using the B1, B2 and B3 bands together. Their results showed that the three-band method ~~may~~ performs better than the two-band method with a root mean square error lower than 1 K.

Considering the benefit of incorporating three thermal infrared bands for observation, ~~Thus, the~~all three bands of SDGSAT-1 TIS ~~data~~ are used for lead detection~~ of ice leads~~ in this study. The georeferenced level-4 TIS data (CBAS, 2022) in the Beaufort Sea and the Laptev Sea ~~in~~ during the spring season of 2022 were collected and ~~manually~~ selected manually ~~for~~with cloud coverage of less than 10% for sea ice lead detection. Four successive scenes grouped ~~scenarios of~~ by the 11 TIS data ~~is~~ are shown in ~~Figure 1~~Fig. 1, and t~~(~~he corresponding information is provided in ~~see~~ Table 3~~ for the data information)~~.

~~First, a~~All digital numbers (*DNs*) are converted into at-sensor radiance using ~~formula~~Eq. (1).

$$L = gain \times DN + bias - bg \;, \tag{1}$$

where the $gain$ ~~gain~~ and $bias$ ~~bias~~ are radiometric calibration coefficients provided by the scientific calibration team, which have included relative and absolute radiometric calibrations; bg is the background radiance of the black body. Then, the BT is calculated from the at-sensor radiance using the Planck function.

Table 2. SDGSAT-1 TIS characteristics and radiometric performance (CBAS, 2022)

Spatial resolution	30 m
Swath width	300 km
Revisit time	11 days
Band wavelengths	B1: 8.0-10.5 µm B2: 10.3-11.3 µm B3: 11.5-12.5 µm
Dynamic range	220 K-340 K
Noise equivalent differential temperature (NEΔT)	0.2 K @300 K
Radiometric calibration accuracy	Absolute radiometric calibration: ≤1K, Relative radiometric calibration: 5%

2.2 Sentinel-1 and Sentinel-2

Sentinel-2 (S2) is a constellation of two satellites~~is formed by two satellites~~, S2A and S2B,~~.~~ ~~B~~both ~~satellites are~~ equipped with a Multispectral Instrument (MSI) with thirteen spectral channels covering the visible, near-infrared ~~wave~~ and shortwave infrared spectral zones (ESA, 2015). Level-1c S2 products provide top-of-atmosphere reflectance processed ~~in~~ with radiometric and geometric corrections in tile form~~.~~, with ~~E~~each tile ~~is~~ being an ortho-image in a 100 by 100 km^2 area. S2 MSI visible ~~green band~~ images at a resolution of 10 m are used ~~for~~ to ~~comparison~~ compare with the leads detected by the TIS in this study for validation. We mainly used the ~~3~~ band 3 (560 nm) ~~image~~data, which offers ~~gives a~~ good discrimination between leads and surrounding sea ice in visual comparisons for the scenarios applied in this study.~~, given that the visible~~

~~spectrum centered at 560 nm gives a good effect (König et al., 2019) for a scene containing sea ice and seawater.~~ Images acquired over the Beaufort Sea and the Laptev Sea in March and April 2022 were collected (see Table 3 for the data information, and ~~see~~ the red squares in ~~Figure 1~~Fig. 1 for their ~~location~~coverage).

Sentinel-1 (S1) is a C-band SAR that operates ~~imaging~~ day and night regardless of the weather. Both S1A and 1B acquire dual-polarization (HH and HV) imagery, covering the vast Arctic region. The S1 extra-wide (EW) swath data ~~have~~ has a swath width of approximately 400 km, with a pixel size of 40 m by 40 m (ESA, 2013). We used the S1 level-1b data in the format of ground range detected medium resolution (GRDM). As S1B has been out of operation ~~work~~ since December 2021, only the S1A data are available ~~in~~ during this study period. Considering that the backscatter values of SAR in different polarizations give different sensitivities for leads fully opened or covered by thin ice, we collected S1A dual-polarization data in the Beaufort Sea on April 3 ~~and 28,~~ in 2022 (see Table 3). The dual-polarization data were radiometrically calibrated, and a false-color composition was performed by assigning the HH, the subtraction of HH by HV, and the HV images to the red, green, and blue channels, respectively.

2.3 MODIS ~~IST~~ products

The MODIS is an instrument onboard the two polar-orbiting satellites, Terra and Aqua, which are part of NASA's Earth Observing System (EOS). ~~The~~ MODIS ~~acquir~~acquires data in 36 discrete spectral bands ~~from~~ that cover the optical to ~~the~~ thermal infrared radiance wavelength region. The swath width of ~~the~~ MODIS is 2330 km. The daily level-2 sea ice products, MOD29 and MYD29, ~~daily level-2 sea ice products~~ include sea ice cover and IST datasets (Hall and Riggs, 2021). Each product contains 5 minutes of swath data observed at a resolution of 1 km. The IST data are retrieved ~~by~~using the split-window technique based on the MODIS 31 and 32 bands, with an accuracy of 1.2-1.3 K (Hall et al., 2004). Cloud masking from the MODIS cloud products for daytime and nighttime (Ackerman et al., 1998) is integrated into the IST retrieval. The IST data produced by MODIS/Terra, i.e., MOD~~0~~29 products, and the MOD03 geolocation product (MODIS Characterization Support Team, 2017) are used in this study~~The MOD29P1D and MYD29P1D daily level-3 sea ice products include daily sea ice cover and IST datasets (Hall and Riggs, 2021). Each product contains a tile of data gridded into the Lambert azimuthal equal-area map projection, which is approximately 1200 by 1200 km² in area. The IST datasets have a spatial resolution of 1 km. The IST data are retrieved by the split-window technique based on the MODIS 31 and 32 bands, with an accuracy of 1.2-1.3 K (Hall et al., 2004). Cloud masking from the MODIS cloud products for daytime and nighttime (Ackerman et al., 1998) is integrated into the IST retrieval. Given that the SDGSAT-1 mainly passes over the Laptev Sea and the Beaufort Sea in the morning, IST data produced by MODIS/Terra, i.e., MOD029P1D products, are mainly used in this study~~ (see Table 3 for data information).

2.4 ERA5 air temperature data

The European Centre for Medium-Range Weather Forecasts (ECMWF) provides the fifth-generation reanalysis data (ERA5) for global climate and weather for the past seven decades (Hersbach et al., 2018). The ERA5 near-surface air temperature (2 m air temperature) data is available ~~by every 6~~ hourly~~s~~ ~~and~~ in a regular grid of 0.25 degrees. In this study, we used 2 m air temperature data for the period between March and April 2022~~from March to April 2022~~ to explore ~~analyze~~ the possible variations in the atmospheric environment.

2.5 OMI/Aura product

Since the TIS B1 band (8.0-10.5 µm) corresponds to ~~covers~~ an absorption channel for ozone (Wan and Li, 1997), we analyzed the potential ~~possible~~ absorption effects of different ozone ~~re~~solutions on thermal infrared radiation in this study. The Ozone Monitoring Instrument (OMI) is an instrument onboard the EOS Aura mission. The OMI measurements cover a spectral region of 264–504 nm, which aims to continue the~~-~~ record for total ozone and other atmospheric parameters related to ozone chemistry and climate. The total column ozone is retrieved based on the long-standing TOMS V8 retrieval algorithm (Bhartia, 2002), which uses a weakly absorbing wavelength (331.2 nm) to estimate an effective surface reflectivity and another wavelength (317.5 nm) with stronger ozone absorption to estimate ozone. The level-3 OMI/Aura Ozone Total Column data (OMTO3) are produced ~~by~~ using best pixel data from approximately 15 orbits, covering the whole globe and mapped in a grid size of 0.25 degrees (Bhartia, 2012).

Table 3. Information of satellite data and derived product used in this study

		SDGSAT-1 TIS	Sentinel-2 MSI	MOD~~0~~29 and MOD03~~P1D~~	Sentinel-1A EW
Date and time (UTC)	2022-03-23	10:52:13 10:52:59 10:53:43 10:54:13	03:55:34	~~h07/08/09/10 v07/08/09~~10:30 12:05	/
	2022-04-03	04:26:39 04:27:09 04:27:39 04:28:09	21:00:23	~~h07/08/09/10 v07/08/09~~05:10	15:53:09
	2022-04-28	04:56:25 04:55:26 04:55:55	22:42:28	~~h07/08/09/10 v07/08/09~~05:05	/
Spatial resolution		30 m	10 m	1 km	Pixel size: 40 m

3 Method

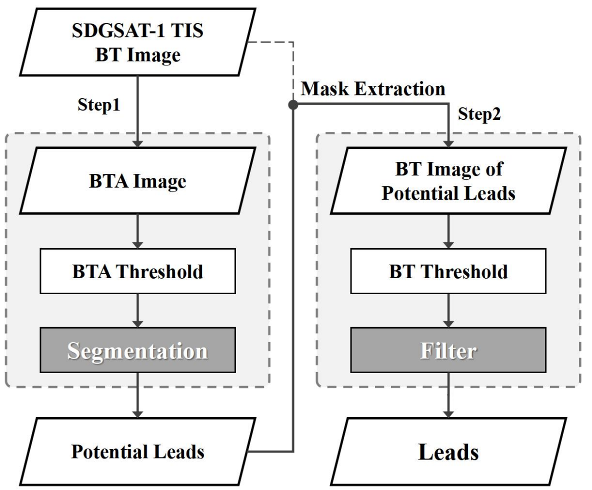

Figure 2: Flowchart of sea ice lead detection based on SDGSAT-1 TIS data.

In this section, we propose a method for sea ice lead detection adaptable to high-resolution TIS images, based on the principle of exploiting both the relative and absolute temperature characteristics of sea ice leads.~~3.2 Detection of ice leads~~ L~~Ice l~~eads containing seawater and thin ice have temperatures higher than the surrounding sea ice. Therefore, detecting leads is based on the ~~the~~ temperature contrast between leads and the sea ice surface~~ is the basis of detecting ice leads~~ (Willmes and Heinemann, 2015a; Hoffman et al., 2019; Qu et al., 2021). However, as the spatial resolution of thermal infrared imagery improves~~is improved~~, the temperature variations in sea ice with different thicknesses pose a challenge for accurate lead identification. To address this issue, the algorithm we proposed mainly involves two steps: a segmentation and a filter, which correspond to the two major steps in the flowchart in ~~Figure 2~~Fig. 2~~ shows the flowchart for detecting leads based on SDGSAT-1 TIS data in this study, which contains a segmentation and a filter.~~. The algorithm's input is the BT data of each TIS band (B1, B2, and B3 bands~~),~~). A representative scenario containing both large and narrow leads, along with surface temperature variations, is presented in ~~as shown in~~ Fig~~ure~~. 3 (a)~~-~~, using the TIS B1 band as an example~~for an example of the B1 band~~. Thanks to the high spatial resolution of 30 m, the thermal features of sea ice and leads are clearly observable. In addition to the leads presenting as distinct yellow and red colors (in the temperature range of 242 K to 252 K) ~~colors~~ on the BT map, slight variations in sea ice surface temperature can be identified from approximately 237 K to 242 K. The brightness temperature anomaly (BTA) images are derived from the BT data by subtracting the mean temperature in neighbouring windows with sizes of 2.4 km by 2.4 km (80 pixels by 80 pixels), as shown in ~~Figure 3~~Fig. 3 (b). Undoubtedly, the BTA data further highlight the presence of leads, but the positive BTA values caused by thinner sea ice are also highlighted. To this end, the first step of our lead detection involves ~~is~~ applying a binary segmentation to extract~~s~~ potential leads from the BTA data. In the second step, the derived potential leads are used together with the BT data to extract the BT values of the potential leads, and then used in a designed filter to obtain the consequent leads.~~A designed filter is further~~

~~applied to the segmentation, and the leads are consequently obtained.~~ The ~~following~~ next two subsections describe the two major steps involved in the proposed method.

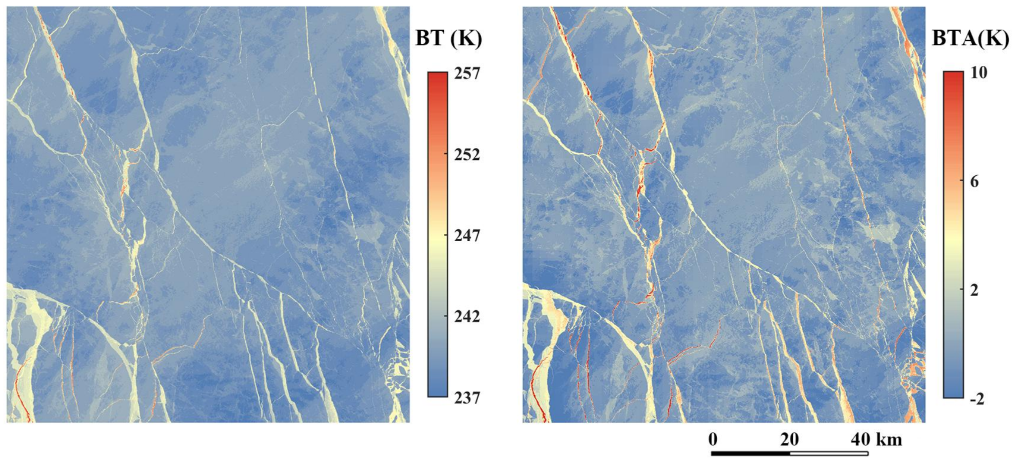

(a) (b)

Figure 3: Example for the BT image and BTA image based on the SDGSAT-1 TIS B1 band (8-10.5 μm) acquired on April 3 in 2022. (a) The BT image. (b) The derived BTA image.
SDGSAT-1 TIS data ID: KX10_TIS_20220403_W128.84_N73.00_202200033226.

3.~~2.~~1 Potential lead segmentation ~~of ice leads~~ based on ~~the~~ BTA data

The key to performing a binary segmentation by the BTA data is to identify ~~find~~ an appropriate threshold to segment sea ice and leads. To achieve this, we collected ~~By collecting~~ ~~eight~~ seven TIS data acquired between April 3 and April 28, 2022 in the Arctic Ocean, ~~we~~ and analyzed the distribution of their BTA data, as illustrated ~~shown~~ in ~~Figure 4~~Fig. 4. The BTA data follow ~~show~~ a normal distribution, as demonstrated by the Gaussian fitting ~~as the overlaid Gaussian fitting~~ (with μ = -0.25 K, σ^2 = 0.38 K) overlaid on the graph~~indicates~~. The ~~peak in the~~ histogram displays a peak ~~appears~~ at -0.25 K, accounting for 15.09% of all the data. The long tail on the positive side of the histogram suggests that the presence of ~~images contain~~ leads in the images, as they have ~~a~~ higher temperatures than the surrounding ~~sea~~ ice. Therefore~~us~~, it is necessary to~~we need to~~ determine a threshold in the positive BTA range to accurately segment the leads from other features.

Previous ~~methods~~ studies applied various~~a variety of~~ BTA thresholds for lead detection (Willmes and Heinemann, 2015a; Hoffman et al., 2019; Qu et al., 2021). For instance, ~~B~~based on BTA derived from the MODIS IST product, Willmes and Heinemann (2015a) compared the standard deviation and ~~a set of~~ non-parameterized methods. In terms of BTA derived by MODIS 11 μm swath data, Hoffman et al. (2019) identified a threshold of 1.5 K. Qu et al. (2021) took 1.2 K, 1.5 K and 2 K as thresholds for different types of leads, corresponding to large to small uncertainty levels. We enlarged a part of the histogram tail in ~~Figure 4~~Fig. 4 and observed that ~~. T~~the Gaussian curve gradually deviates from the bars when the BTA value exceeds ~~is greater than~~ 1.2 K, ~~which should~~ indicating~~e~~ a transition from ice to leads. We tested various thresholds and found that selecting ~~choosing~~ 1.2 K, 1.8 K, and 2.7 K as thresholds ~~yields~~ results in distinguishable differences in the segmentation results, as illustrated ~~one example presented~~ in ~~Figure 5~~Fig. 5. Using a threshold of 1.2 K results in false-positive detections (i.e., sea ice or other~~s~~ features classified as leads), as exemplified by~~e.g.,~~ the white pixels marked by the orange square in ~~Figure 5~~Fig. 5 (a) (this can be identified in the original BTA map shown in ~~Figure 3~~Fig. 3 (b)). In contrast, using 2.7 K as the threshold causes~~results in a~~ loss of detail, ~~e.g.,~~as highlighted by the part marked by the orange square in ~~Figure 5~~Fig. 5 (c) (compared to ~~Figure 5~~Fig. 5 (b)). Multiple threshold segmentation was tested ~~when the~~by varying the BTA threshold ~~was varied~~ from 1.2 K to 2.7 K in 0.1 K steps. After visual comparison, we found that using 1.8 K as the threshold yields ~~presented~~ a significantly different segmentation effect, which ~~can~~ ~~Multiple tests using 1.8 K as the BTA threshold~~ avoids~~s~~ many false-positive detections while still capturing lead details, as demonstrated in Fig. 5 (b). Therefore, ~~. The~~a BTA threshold of 1.8 K was applied to all SDGSAT-1 TIS data in this study for potential lead segmentation.

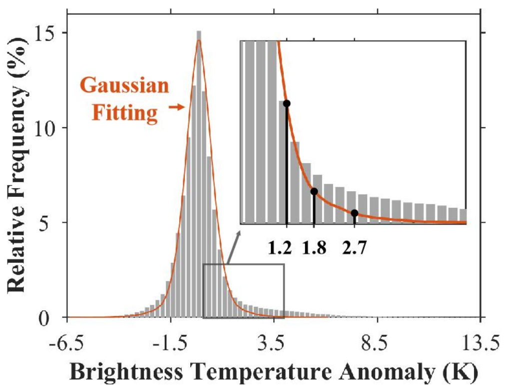

Figure 4: Statistical BTA histogram of seven TIS data acquired from April 3 to April 28, 2022, with a bin width of 0.25 K. The orange curve is the Gaussian fitting, with μ = -0.25 K and σ^2 = 0.38 K.

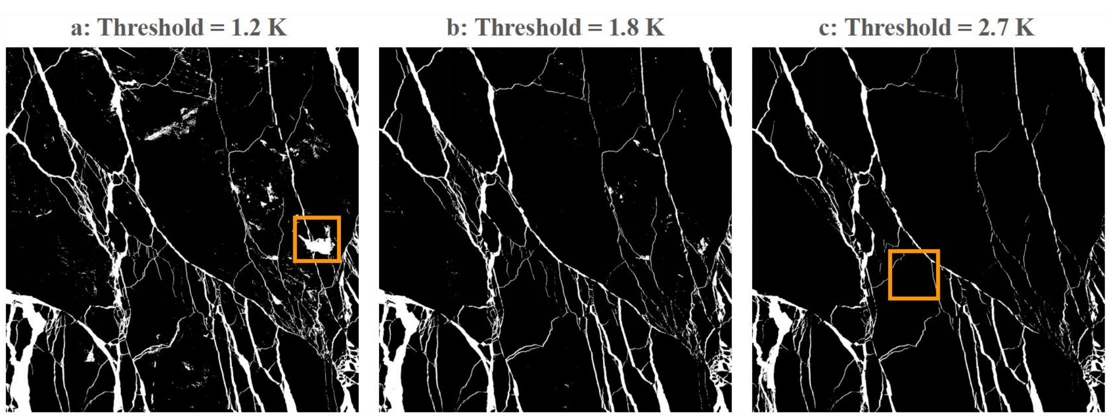

Figure 5: BTA threshold tests for potential lead segmentation using the thresholds of 1.2, 1.5 and 2.7 K (left to right). BTA values greater than or equal to the threshold are classified as 1 (white areas) and values less than the threshold are assigned 0 (black background). Orange squares indicate false detections.

3.~~2.~~2 Further filter based on a BT threshold

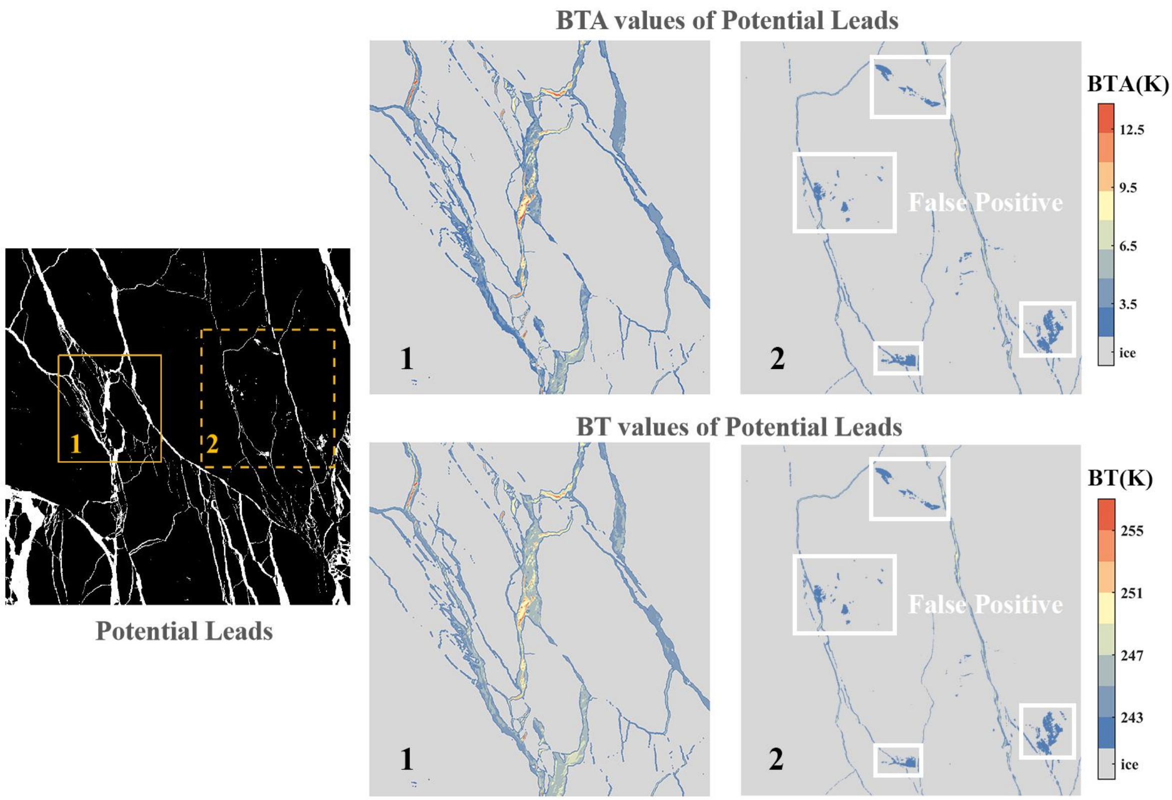

Figure 6: Characteristics of potential leads after segmentation ~~based on the TIS B1 image~~. The left panel presents a binary image ~~on the left panel~~of ~~presents the~~ potential leads detected by segmentation (the same as Fig. 5 (b)),~~,~~ with ~~where t~~the two squares ~~are~~ highlighted: view 1 represents~~:~~ highly reliable detection, ~~and~~ while view 2 is~~:~~ part of a false-positive detection. Corresponding to the two views, the right panel displays the BTA images of ~~For~~ these potential leads in ~~both~~ the first row and the ~~views, their BTA images are shown in the first row on the right panel, and the~~ BT images ~~are shown~~ in the last row, w~~here~~ith the gray background representings the ~~the~~ ice surface.

SDGSAT-1 TIS data ID: KX10_TIS_20220403_W128.84_N73.00_202200033226.

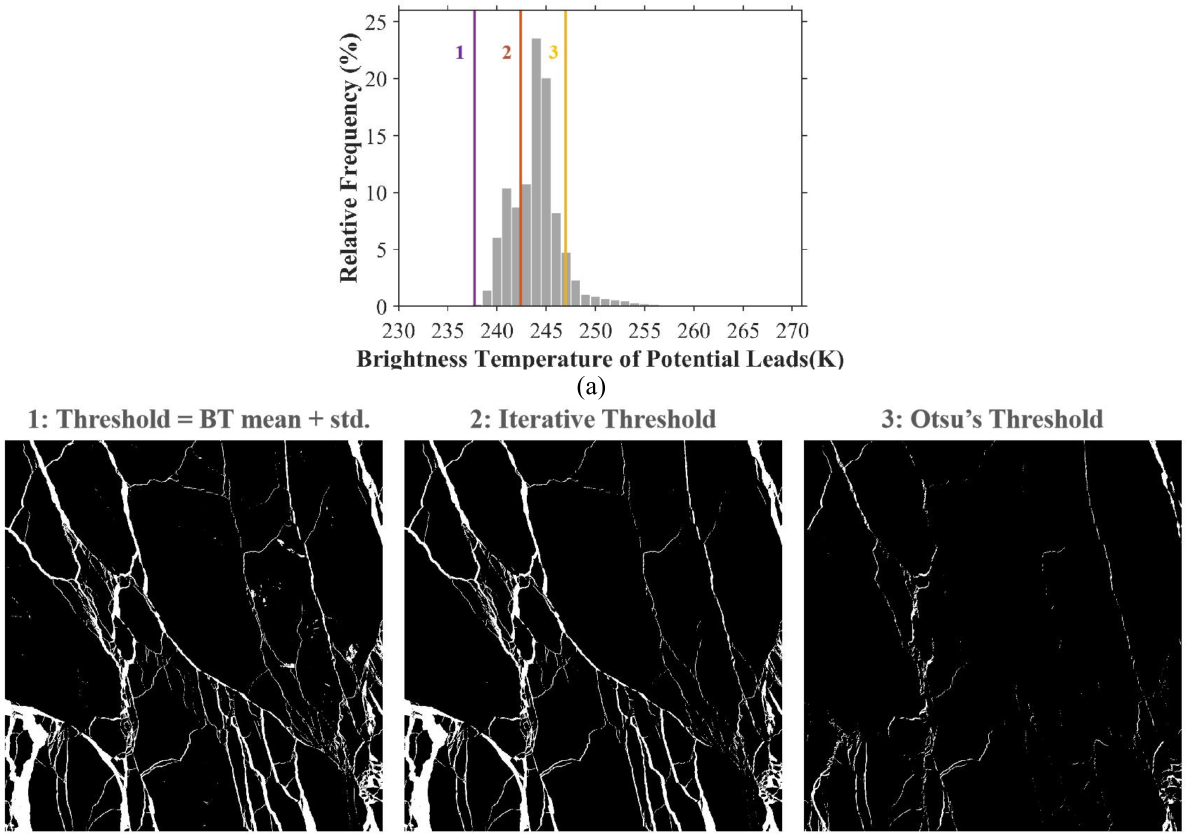

(b)

Figure 7: BT threshold tests and filtered results~~ based on~~ by ~~the~~ different thresholds~~.~~, 1: mean plus standard deviation (std.) of BT before segmentation, 2: iterative threshold, and 3: Otsu's threshold. (a) BT histogram of potential leads~~ overlaid,~~ with the overlaid three lines indicating the three BT thresholds ~~selections~~ selected for the ~~BT threshold~~ ~~of the~~ filter.~~-~~ (b) The filtered results by the three thresholds, where the pixels with BT values below the threshold are rejected and classified as background. ~~These thresholds are 1: mean plus standard deviation (std) of BT before segmentation, 2: iterative threshold, and 3: Otsu's threshold.~~

SDGSAT-1 TIS data ID: KX10_TIS_20220403_W128.84_N73.00_202200033226.

After conducting ~~Following~~ the segmentation ~~conducted~~ in the previous step, a few false-positive detections remain in the result. False positive detections can be attributed to imperfectly removed clouds, cloud edges, or sea ice of different thicknesses~~This situation is unavoidable to some extent because masses of information on the sea ice surface are also resolved by high-resolution thermal infrared data~~. ~~Even small~~These interferences ~~changes~~ cause gradient variations in the BT values measured by the TIS sensor,~~in the temperature gradient~~ ~~could~~ resulting in ~~yielding~~ high BTA values~~,~~. To improve the detection accuracy, we~~resulting in false-positive detections. We~~ decided to identify the reliability of those potential leads~~ for better detection accuracy~~. I~~O~~n the left panel of ~~Figure 6~~Fig. 6, the potential leads within the square marked by solid yellow lines (in view 1) are considered reliable, while part of the white pixels marked by the other square ~~(~~with dashed lines~~)~~ (in view 2) are false-positive detections. The right parallel panels of Fig. 6 show t~~T~~he BTA and BT data of the ~~detected~~ potential leads ~~in~~ for the two views ~~are displayed in the first row on the right panel, and the corresponding BT data are shown in the next row~~. Whether for the first-row BTA or second-row BT data, the dark blue pixels (marked by white squares) are more likely to represent ~~those~~ false-positive detections. However, it is difficult to evaluate further the reliability of potential leads based ~~on~~ only on the BTA data, as both views in the first row have BTA values close to dark blue with no significant differences. In contrast, false-positive detections ~~can~~ could be easily distinguished from leads based on the BT data. For example, in the second row of right parallel panels, the absolute values of the BT of ~~those~~ reliable leads in the first column (~~in~~ view 1) are all greater than those of the false-positive detections in the second column (~~in~~ view 2) by at least 2 K.

The BT histogram for ~~those~~ the ~~remaining~~ potential leads is shown in ~~Figure 7~~Fig. 7 (a). Th~~os~~e pixels with low temperature on the left side represent the false-positive detections; the high-frequency pixels and the tail on the right represent ~~are those~~ highly reliable leads. Thus, we used a filter to remove the pixels with BT values below a given threshold. Unlike ~~using~~ the BTA threshold as a constant, the threshold determined for the BT data is adaptive for environmental variations. In this regard, we tested non-parameterized threshold selection methods, including Otsu’s threshold (Otsu, 1979), iterative selection (Ridler and Calvard, 1978), and the threshold based on the BT mean and standard deviation (calculated by the BT map before segmentation). The selected thresholds are shown as the three lines in Fig. 7 (a), and ~~T~~the ~~result~~ filtering results using these thresholds in ~~Figure 7~~Fig. 7 (b) suggest~~s~~ that the iterative threshold filter performs the best ~~because~~ in~~it~~ ~~rejects~~ rejecting false detections. The mean and standard deviation filter ranks second. ~~The~~ Otsu’s threshold is not adapted for ~~use in~~ this filter. Therefore, we chose the iterative selection as the method to determine the BT threshold in this filter~~the iterative selection determines the BT threshold in this filter~~. The starting position of the iteration is set to the sum of the BT mean and standard deviation, which can save iterative times. For each TIS band, the respective threshold was selected, and the pixels with BT values below the threshold ~~was~~ were filtered out. Finally, three binary results at 30 m resolution were derived separately from each of the three bands of the SDGSAT-1 TIS.~~Finally, the binary detection of leads at a 30 m resolution was derived based on SDGSAT-1 TIS in three bands.~~

4 Results

This section presents the derived sea ice leads at a 30 m resolution based on SDGSAT-1 TIS data in the Arctic Ocean and detailed comparisons with the S2 data and with the MODIS-derived leads, as well as the cross-comparisons among the three bands. The results are based on a total of 11 TIS data that are grouped into four scenes and have three sub-regions for matching comparison with the S2 (see ~~Figure 1~~Fig. 1).

4.1 Comparison of ~~the~~ TIS-detected sea ice leads with Sentinel-2 images

To assess ~~examine~~ the reliability of sea ice leads detected in this study, we ~~first~~ conducted a ~~carried out~~ comparison~~s~~ of typical cases under clear sky conditions. T~~he t~~wo cases ~~presented below are~~ in the Beaufort Sea near the Canadian Arctic Archipelago are presented, as ~~. S~~sea ice leads in this region exhibit ~~have~~ typical seasonal variations (Steele et al., 2015). Here, we focused on the leads detected in April 2022 (marked by ~~in the~~ red squares on borders 1 and 2 in ~~Figure 1~~Fig. 1) and validated them using co-located~~.~~ S2 MSI visible images~~ were col-located with the derived leads for validation~~. The ~~three BT maps are displayed in the~~ first row of ~~Figure 8~~Fig. 8 displays the three BT maps~~.~~, with ~~T~~the detected leads ~~in this study are~~ represented by the white pixels in the ~~following~~ binary maps that follow. For the matched visible images, ~~the albedo of a lead is lower than that of the sea ice surface, so~~ leads are ~~the~~ darker than the ice surface~~ objects in the S2 images~~. According to ~~the~~ a previous ~~lead~~ study based on leads using S2 data (Muchow et al., 2021), we calculated the normalized brightness and determined ~~specified~~ that a pixel with a normalized brightness below 0.7 could be a lead, while a pixel with a normalized brightness above 0.07 could be sea ice. ~~Thus, a p~~Pixels with ~~a~~ normalized brightness between 0.07 and 0.7 is considered to have both possibilities. Apparently, our detection results based on the three infrared bands are highly consistent with these visible images. In particular, it is likely that some of the narrow leads we detected, with widths of tens of meters, have just ~~begun to~~ formed, which are also subtle in 10 m resolution visible images.

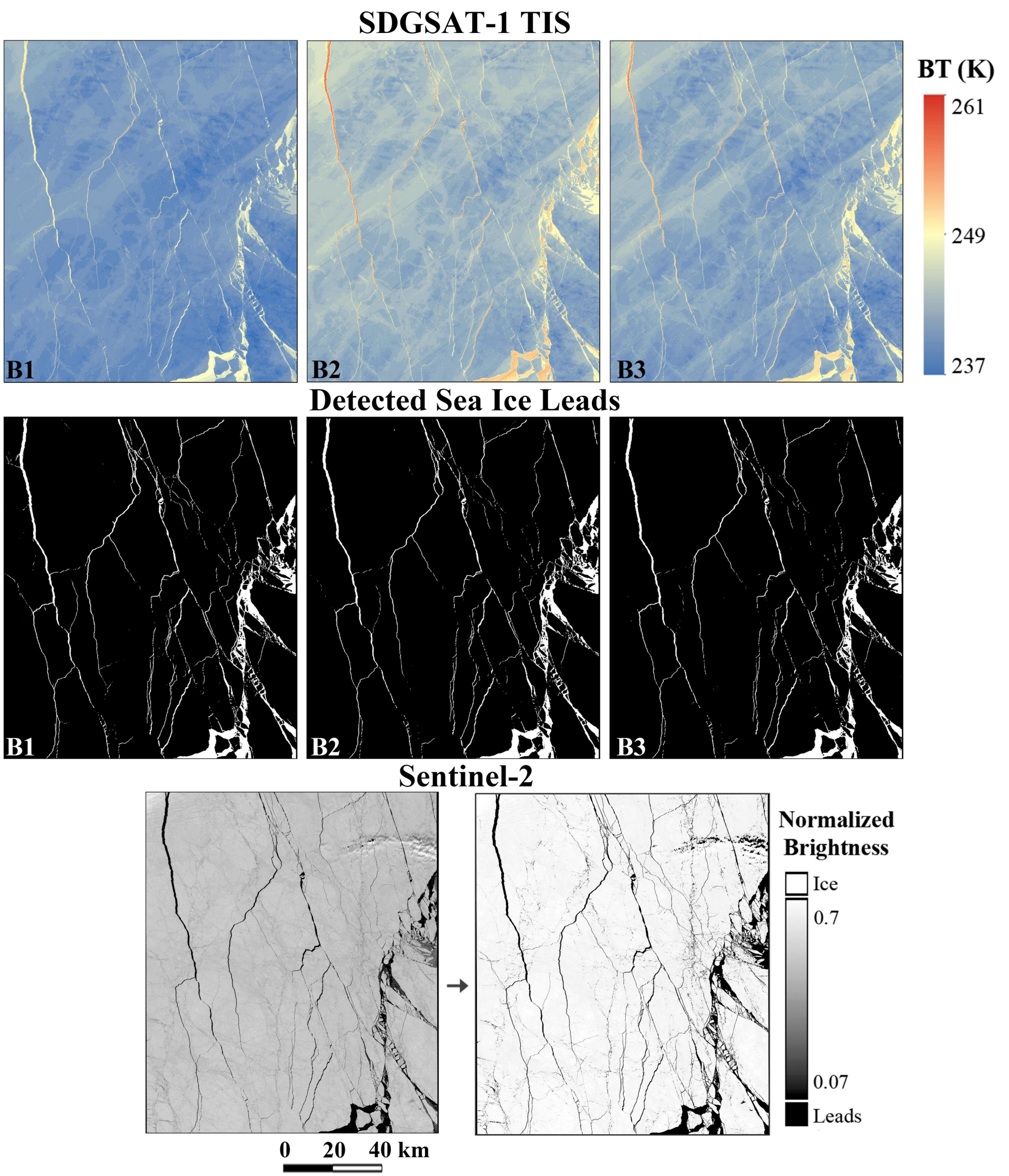
SDGSAT-1 TIS
BT (K)
261
249
237
B1
B2
B3
Detected Sea Ice Leads
B1
B2
B3
Sentinel-2
Normalized
Brightness
Ice
0.7
0.07
Leads
0 20 40 km

(a)

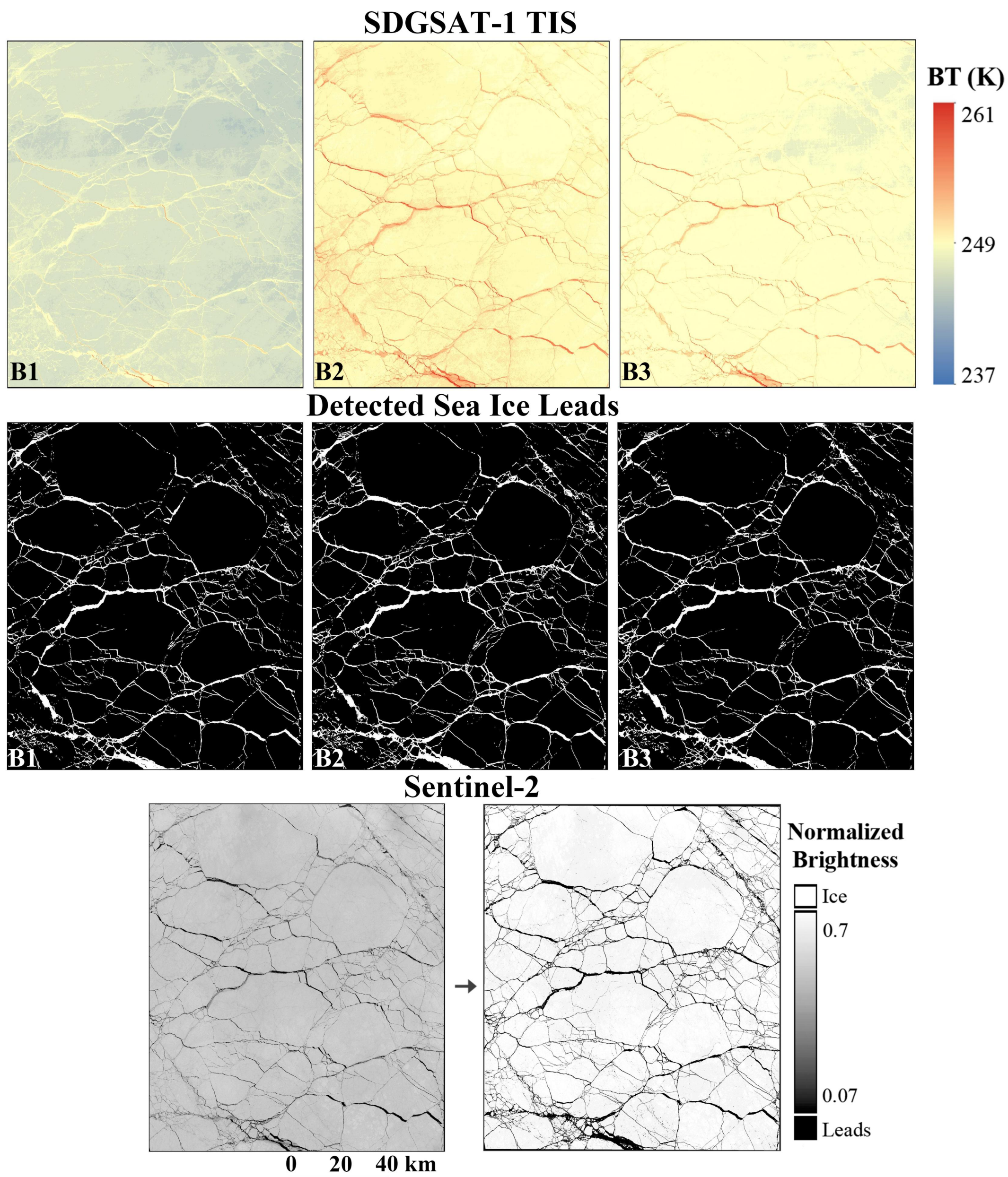

(b)

Figure 8: Validation of sea ice lead detection based on SDGSAT-1TIS data compared with S2 visible images in the Beaufort Sea, April 2022. ~~The three r~~Rows show the BT maps for the B1, B2 and B3 bands, ~~their~~ the lead detection results, the S2 images and the normalized brightness (from 0.07 to 0.7)~~, respectively~~. (a) TIS data acquired at 04:28 UTC and S2 data ~~acquired~~ at 21:00 UTC on April 3, 2022. IDs: KX10_TIS_20220403_W128.84_N73.00_202200033226, KX10_TIS_20220403_W132.14_N74.67_202200033227. (b) TIS data acquired at 04:56 UTC and S2 data acquired at 22:42 UTC on April 28, 2022. ID: KX10_TIS_20220428_W147.26_N77.60_202200049406.

We performed a pixel-by-pixel ~~compared~~ comparison between the TIS-based ~~ice~~ leads ~~with~~ and ~~the~~ visible images ~~on a pixel-by-pixel basis~~. ~~The definitions of TP (True Positive), FP (False Positive), FN (False Negative), and TN (True Negative) used are listed i in~~ Table 4 lists the definitions of TP (True Positive), FP (False Positive), FN (False Negative), and TN (True Negative) used in this study. Due to the imbalance between the distribution of leads and the ice background, we used three indicators ~~for~~ to evaluate the detection performance: ~~the~~ commission error, ~~the~~ omission error, and ~~the~~ accuracy. The statistics listed in Table 5 for the two cases in the Beaufort Sea show that, for all bands, the commission error, omission error, and accuracy are 5.5~~45~~%, 44.7~~3~~%, and 96.3~~0~~%, respectively. The overall accuracy f~~F~~or the three bands~~,~~ ~~the overall accuracy~~ achieves a high level of 96.24%, 96.34% and 96.3~~3~~%, respectively. The B1 band ~~is~~ shows satisfactory results with ~~in terms of~~ an overall commission error of 5.4~~39~~%, but yields a slightly high miss rate of 46.3~~25~~%. The omission error mainly attributes to a large FN result, resulting from ~~subtle~~ refrozen leads ~~(~~covered by thin ice~~)~~. More specifically, the case on April 3 (shown in ~~Figure 8~~Fig. 8 (a)) yields a commission error less than 4.6~~0~~%, while the commission error on April 28 is slightly higher than the former. The reason lies in the differences in the lead distribution ~~and fraction~~. For the ~~April 28~~ case April 28 (shown in ~~Figure 8~~Fig. 8 (b)), more leads ~~that~~ undoubtedly exacerbate the difficulty in detection ~~are presented~~.

Moreover, the BT values recorded by SDGSDAT-1 TIS on these two days were different. Even in the overlapping region of borders 1 and 2 in ~~Figure 1~~Fig. 1, the BT on April 28 is approximately 5 K higher than that on April 3. This finding may imply a short-term temperature variation ~~in temperature on a short temporal scale~~ in the late spring, allowing for the formation of more leads and exhibiting more intricate lead networks. On the other hand, a warming environment can reduce the contrast in thermal infrared data, resulting in lower BTA values for leads. The phenomenon is related to different atmospheric conditions, which we further analyze in the Discussion.

~~By a~~Applying this detection method to the TIS data acquired over the Laptev Sea on March 23, 2022 (shown within rectangle 3 in ~~Figure 1~~Fig. 1), we found a complex situation when compared to the S2 visible image, as shown in Fig.~~ure~~ 9. The expansive gray feature on the S2 images is more likely to be cloud shadow than leads (McIntire and Simpson, 2002). Detecting leads under this interference is quite challenging ~~difficult~~ since the thermal contrast is far less distinct than that on a clean ice surface, as shown in the following BTA maps. Compared to the visible image, the accuracy values for the B1, B2 and B3 bands are 95.5~~3~~%, 95.4~~3~~%, and 95.~~56~~6%, respectively. However, some FP detections remain in the three bands, which are marked by yellow rectangles in the third row. Thus, although this detection based on SDGSAT-1 TIS data show promising applicability, the uncertainty caused by cloud interference remains to be further explored.

Table 4. Definition of comparison ~~a pixel-by-pixel~~ result~~s comparison~~ of~~for~~ the binary lead detection ~~and~~ with the ~~optical~~ visible images with normalized brightness.

		Normalized brightness of the S2 visible image	
		< 0.7	**> 0.07**
Leads detection	**1**	TP (True Positive, sea ice leads)	FP (False Positive)
	0	FN (False Negative)	TN (True Negative, sea ice)

405

Table 5. Lead detection performance based on the TIS data in the Beaufort Sea on April 3 and 28, 2022. Results from each TIS band are aggregated into overall results, which are then aggregated ~~and from all TIS bands~~into the all-band results.~~ are aggregated~~

		Commission Error (%)	Omission Error (%)	Accuracy (%)
		$\frac{FP}{TP + FP}$	$\frac{FN}{FN + TP}$	$\frac{TP + TN}{TP + TN + FP + FN}$
April 3	B1	4.~~56~~6	45.94	96.3~~1~~
	B2	~~3.99~~4.0	47.~~39~~4	96.3~~28~~
	B3	3.9~~3~~	47.7~~3~~	96.3~~26~~
April 28	B1	6.7~~0~~	46.7~~3~~	96.1~~2~~
	B2	7.~~28~~3	38.~~86~~9	96.44
	B3	7.~~28~~3	38.7~~1~~	96.4~~3~~
Overall	B1	5.~~39~~4	46.~~25~~3	**96.24**
	B2	5.~~48~~5	43.9~~1~~	**96.34**
	B3	5.~~47~~5	44.04	**96.3~~3~~**
	All Bands	**5.~~45~~5**	**44.7~~3~~**	**96.3~~0~~**

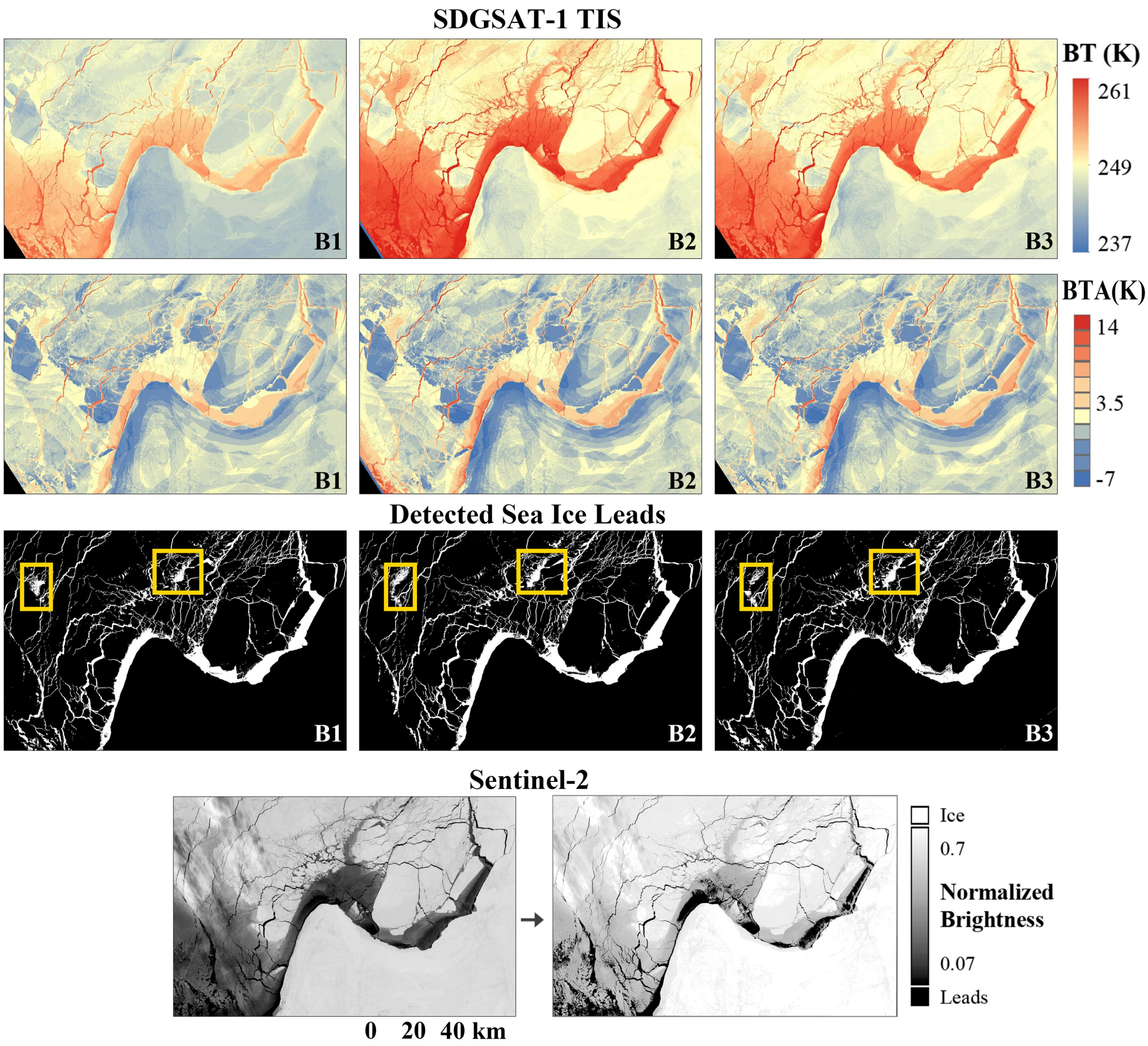

Figure 9: Application of the lead detection method to the SDGSAT-1 TIS data acquired over the Laptev Sea at 10:53 UTC on March 23, 2022, and comparison with the S2 visible image at 03:55 UTC on the same day (similar illustration to the previous figure). IDs: KX10_TIS_20220323_E129.38_N75.60_202200028841 and KX10_TIS_20220323_E133.08_N73.96_202200028843

4.2 Cross-comparison of sea ice lead detection based on the three TIS infrared bands

The three TIS bands all yield good accuracy in lead detection but do present some discrepancies. In this subsection, we performed cross-comparisons of these results to focus on the effectiveness of the three thermal infrared bands in detecting leads. Counting the lead pixels derived from each TIS band, a total of 46,301,986 pixels comprise the consistency detection (co), i.e., a pixel that is detected as a ~~ice~~ lead~~s~~ from all three bands. Thus, the additional detection (ad) is calculated (i.e., detected as a ~~ice~~ lead~~s~~ by a specific band) using ~~formulas~~ Eq. (2) and Eq. (3).

$$N_{Bn,\,ad} = N_{Bn} - N_{co} \,, \tag{$\cancel{1}2$}$$

$$P_{Bn,\,ad} = N_{Bn,\,ad} / N_{co} \times 100\% \,, \tag{$\cancel{1}3$}$$

where N is the total number of pixels; Bn is the infrared band (n = 1, 2, 3); and P is the proportion. The results listed in Table 6 show that the additional detections from the B1, B2 and B3 bands account for 11.46%, 23.30%, and 21.88%, respectively. The fewest leads are detected by the B1 band, while the B2 and B3 bands give similar results.

Table 6. Statistics of lead pixels detected based on the three infrared bands of the SDGSAT-1 TIS

	Leads Pixels Number	**Additional detection**	
		Pixels Number	**Proportion**
B1	51,609,678	5,307,692	11.46%
B2	57,088,756	10,786,770	23.30%
B3	56,430,724	10,128,738	21.88%
Consistency	46,301,986		

To further investigate the discrepancies, we depicted the detections with different colors. As depicted ~~shown~~ in ~~Figure 10~~Fig. 10, dark red, orange and dark blue colors ~~mark~~ represent the leads detected by the B1, B2, and B3 bands, respectively. The discrepancies primarily occur in the lead margins~~ of leads~~. Comparisons in the second (B1 vs. B2) and fourth columns (B1 vs. B3) in ~~In Figure 10~~Fig. 10 (a)~~, the comparisons in the second (B1 vs. B2) and fourth columns (B1 vs. B3)~~ indicate that the B1-derived leads are generally less than those from the B2 and B3 bands. The third column (B2 vs. B3) presents only a small number of spatial variations, probably due to local temperature gradients. Thus, it can be concluded that the TIS B2 and B3 bands yield ~~almost~~ comparable performances in detecting sea ice leads. These two infrared radiance bands, applied as the two split windows for temperature retrieval, are widely used in infrared sensors, e.g., the currently in-orbit Gaofen-5 (GF-5) Visual and Infrared Multispectral Sensor (VIMS), Landsat-8 TIRS, Landsat-9 TIRS-2, and Terra/Aqua MODIS. However, the scenario ~~example~~ in ~~Figure 10~~Fig. 10 (b) shows a different situation~~scenario~~. There are more dark red pixels in the cross-comparisons. In particular, some dark red pixels (marked by the black squares) are only presented in the B1 band results, while the B2 and B3 bands almost lose all this information. Figure 10 (c) shows the S2 visible images acquired in the same location, where the lead characteristics are evident (marked by white squares). Indeed, the BT and BTA maps found no apparent differences in the lead thermal characteristics. It is speculated that the missing data in the B2 and B3 bands may result from interference induced by strip noise, which is particularly pronounced in the two bands (a similar phenomenon is also presented in the split-window channels of MODIS and Landsat 8 TIS). Regardless, this example suggests that using the TIS B1 band appears to achieve unexpected effects in the presence of interference in B2 and B3 data. In other words, the B1 band can be complementary to the two split-window bands. Thus, combining the results of the three bands is beneficial for resolving ~~the~~ narrow leads with better accuracy.

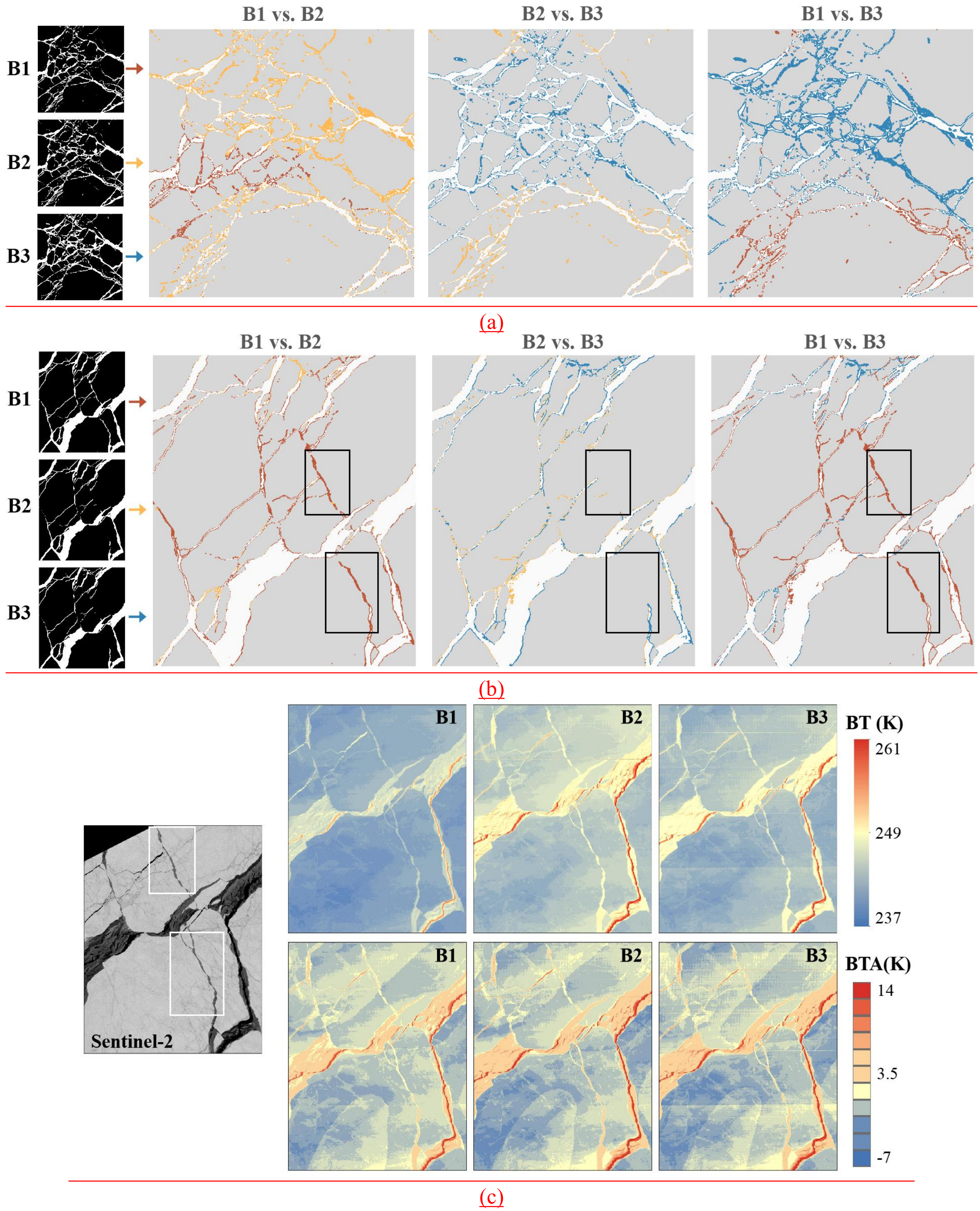

Figure 10: Cross-comparisons of lead detections ~~between the detections~~ among ~~the~~ three TIS ~~infrared~~ bands. The first column in (a) and (b) shows ~~the lead~~ detections by the three bands. The following three columns are the pairwise comparisons, ~~where~~ with dark red, orange, and dark blue representing the B1, B2, and B3 results, respectively.~~the dark red, orange, and dark blue pixels~~

~~represent the B1-derived and B2-derived B3-derived results, respectively.~~ White pixels are~~is~~ ~~the~~ consistency detections, and ~~the~~ light gray ~~background is~~indicates ~~the~~ ice surface. Acquired from the same location as (b), the left panel in (c) shows the S2 image as ~~a~~ reference, ~~and~~ with BT and BTA maps in two parallel rows~~the two parallel rows of panels are the BT and BTA maps for the three bands~~. (a) TIS data acquired at 04:56 UTC on April 28. ID: KX10_TIS_20220428_W147.26_N77.60_202200049406. (b) and (c) TIS data acquired at 04:28 UTC on April 3. ID: KX10_TIS_20220403_W132.14_N74.67_202200033227. (c) S2 data acquired at 21:00 UTC on April 3.

4.3 Comparison of the TIS-derived sea ice leads with the MODIS

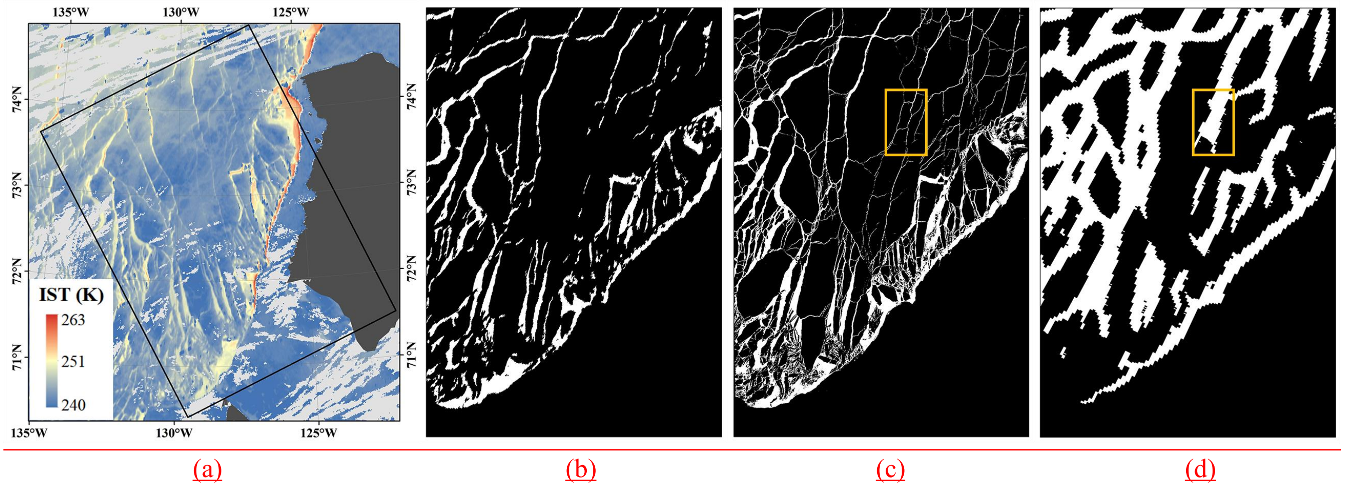

Figure 11: Comparisons ~~between~~ of lead detections ~~based on~~from MODIS data and SDGSAT-1 TIS data in the Beaufort Sea on April 3, 2022. (a) MODIS IST product~~s, where~~ with off-white clouds~~the clouds are off-white~~, dark gray ~~the~~ land~~ is dark gray~~, and ~~the~~ overlaid black border ~~denotes~~ denoting ~~a~~ coverage for (b), (c) and (d). (b) Leads detections at 1 km resolution ~~derived by~~from MODIS IST~~ product~~. (c) Lead detections ~~Leads~~ at 30 m resolution ~~derived~~ from the combined result of ~~SDGSAT-1~~ TIS B1, B2 and B3 bands. IDs: KX10_TIS_20220403_W126.10_N71.30_202200033225, KX10_TIS_20220403_W128.84_N73.00_202200033226, KX10_TIS_20220403_W132.14_N74.67_202200033227. (d) Lead detections ~~Leads~~ at 1 km resolution ~~derived by~~from Hoffman et al. (2022b).

Table 7. ~~Statistics of the l~~Lead areas estimated from the MODIS IST data, ~~and~~ the SDGSAT-1 TIS data and Hoffman et al. (2022b).

		Sea ice lead area (km^2)			Additional lead area by the TIS than by Hoffman et al. (2022b) (km^2)
		MODIS IST	SDGSAT-1 TIS	TIS/MODIS IST	
1	Beaufort Sea on April 3	14,283	15,362	~~1.15~~1.08	5,679
2	Beaufort Sea on April 28	4,238	10,500	2.48~~6.48~~	4,590
3	Laptev Sea on March 23	4,021	4,519	~~1.10~~1.12	1,462
4	Laptev Sea on March 23	3,886	3,936	~~1.01~~1.01	2,415
	Total	**26,427**	**34,318**	**1.30~~1.50~~**	**14,145**

We further compared the TIS-derived ~~ice~~ leads with the MODIS IST data at a moderate resolution. To achieve a fair comparison between the two sensors, we used analogous methods, as shown in a case study in the Beaufort Sea on April 3, 2022, depicted in ~~As one case in the Beaufort Sea on April 3, 2022 presented in Figure 11~~Fig. 11 (a)~~,~~. T~~t~~he IST products were used to derive the BTA maps and ~~then~~ applied a BTA threshold of 1.5 K for binary segmentation (Qu et al., 2021), which is also based on fixed thresholds (~~similar~~thus analogous to our proposed method). ~~Thus, the use of analogous methods allows for a fair comparison of the differences in lead observation between the two sensors. T~~The MODIS-derived lead map is shown in ~~Figure 11~~Fig. 11 (b). Concurrently~~Simultaneously~~, as per the findings in Sect. 4.2, we combined our three lead maps, based on the three TIS bands, into one binary map, ~~in which~~where the combined pixel is positive as long as any one of the three maps yields ~~gives~~ a positive pixel. The combined map contains the most leads,~~We further compared the TIS-derived ice leads with the MODIS data at a moderate resolution. The previously developed method (Qu et al., 2021) was applied to detect the leads based on the MODIS IST data. The IST products in March and April 2022 were first mosaicked (as one case in the Beaufort Sea on April 3, 2022 presented in Fig. 11 (a)) and then applied to the binary segmentation by a BTA threshold of 1.2 K to derive the lead data (the corresponding result is shown in Fig. 11 (b)). Simultaneously, we combined the lead detections based on the three TIS bands, and the result is one binary map containing the most leads~~ as shown in~~(see~~ ~~Figure 11~~Fig. 11 (c)~~)~~. There is a significant difference between the high- and moderate-resolution results. The TIS resolves more lead details, e.g., the narrow leads connecting ~~those~~ wide ones. Furthermore~~Notably~~, some of the leads in ~~Figure 11~~Fig. 11 (c) are even obtained in ~~places~~ areas ~~that are~~ considered clouds by the MODIS cloud mask. Cloud-masked pixels were not compared for consistency purposes~~For the sake of unity, no comparisons were made in the cloud-masked pixels~~.

Correspondingly, the lead area was calculated ~~by~~ from ~~the~~both ~~two~~ datasets in the same regions, as shown in~~.~~ ~~For~~ the four regions ~~shown~~ in ~~Figure 1~~Fig. 1, and the comparison~~s~~ results ~~of the ice lead areas~~ are listed in Table 7. The area estimated from the TIS data is significantly larger than that estimated from MODIS IST, with the total area being 1.3 times larger than the latter.~~exceeding the latter by more than half.~~ In particular, the difference ~~of~~ in the lead area between the TIS and MODIS ~~reaches~~ is the most significant ~~its maximum in~~for ~~the comparison of~~ the case study in the Beaufort Sea on April 28. The leads detected by the TIS are 10,500 km^2 in area (with the B1, B2 and B3 bands of 7,752 km^2, 9,346 km2 and 8,973 km^2, respectively). This could be attributed to the temperature variations on a short temporal scale. The IST increases to approximately 260 K in the Beaufort Sea on April 28, far beyond the general IST range of ~~from~~ 240 K to 250 K for the study area (also see ~~Figure 12~~Fig. 12 (a)). Consequently, the reduced thermal contrast of leads severely limits the ability of MODIS to detect leads. In contrast, the high-resolution imaging capability and high sensitivity of the SDGSAT-1 TIS can present more significant thermal contrasts of leads and ice.

Furthermore, Hoffman et al. (2022b) published ~~the~~ a lead dataset since 2002 for the season between November through April, which were detected by the U-net model (Hoffman et al., 2021) ~~based on~~from MODIS 11 µm thermal imagery. This dataset has a~~e~~ spatial resolution of ~~the dataset is~~ 1 km~~, which were~~ and report~~ed~~s ~~as~~ daily aggregated detection frequency. As showed in ~~Figure 11~~Fig. 11 (d), the lead widths and areas detected by this dataset are significantly larger, especially as small leads in close are identified as ~~an~~ one entire large lead (see the orange squares marked in ~~Figure 11~~Fig. 11 (c) and (d)). Given that this dataset is not appropriate for direct estimation of lead area, we used it as a mask and only calculated the area for the TIS-derived leads beyond this mask (i.e., the additional area). The statistics are presented in the last column of Table 7. The TIS-derived leads have an additional ~~A total of additional leads derived by the TIS~~area ~~is~~ of 14,145 km^2 compared to that derived by Hoffman et al. (2022b), which is generally in line with the comparison result ~~of~~ between the TIS and MODIS IST~~-comparison (11,407 km^2).~~. Thus, while the moderate resolution sensor ~~is~~may ~~possible to~~ over-represent the width and area of leads, the narrow leads overlooked under the kilometer scale resolution are predominated.~~This result suggests that the overlooked narrow leads by the moderate-resolution sensor are predominant.~~ Since the width of leads strongly influences the turbulent exchange efficiency over them~~the turbulent exchange efficiency over the leads is very strongly determined by their width and area~~, the ~~lead~~ observation of leads at ~~a~~ high spatial resolution is critical ~~essential~~ to achieve ~~an~~ accurate lead width parameterization and ~~to further~~ estimate their thermal effects. These comparisons with moderate-resolution sensor prove that the TIS is a competitive sensor for detecting sea ice leads in polar regions.

5 Discussion

Based on the high-resolution thermal infrared data available from the TIS onboard SDGSAT-1~~ with the high-resolution thermal infrared data available~~, we successfully detected sea ice leads in the Arctic ~~for the first time~~ at 30 m resolution, achieving good results in terms of the detection accuracy, adaptability and ability to characterize narrow details. In this section, we focus on discussing the influence of different atmospheric conditions on uncertainties in TIS leads observation and analyzing the lead~~s~~ ~~properties~~ property revealed in the detection. This will provide insights into the factors affecting the accuracy of the TIS observation and the physical characteristics of the detected leads.

5.1 Atmospheric influence~~s~~ on sea ice lead~~s~~ detection by the three TIS infrared bands~~TIS three bands~~

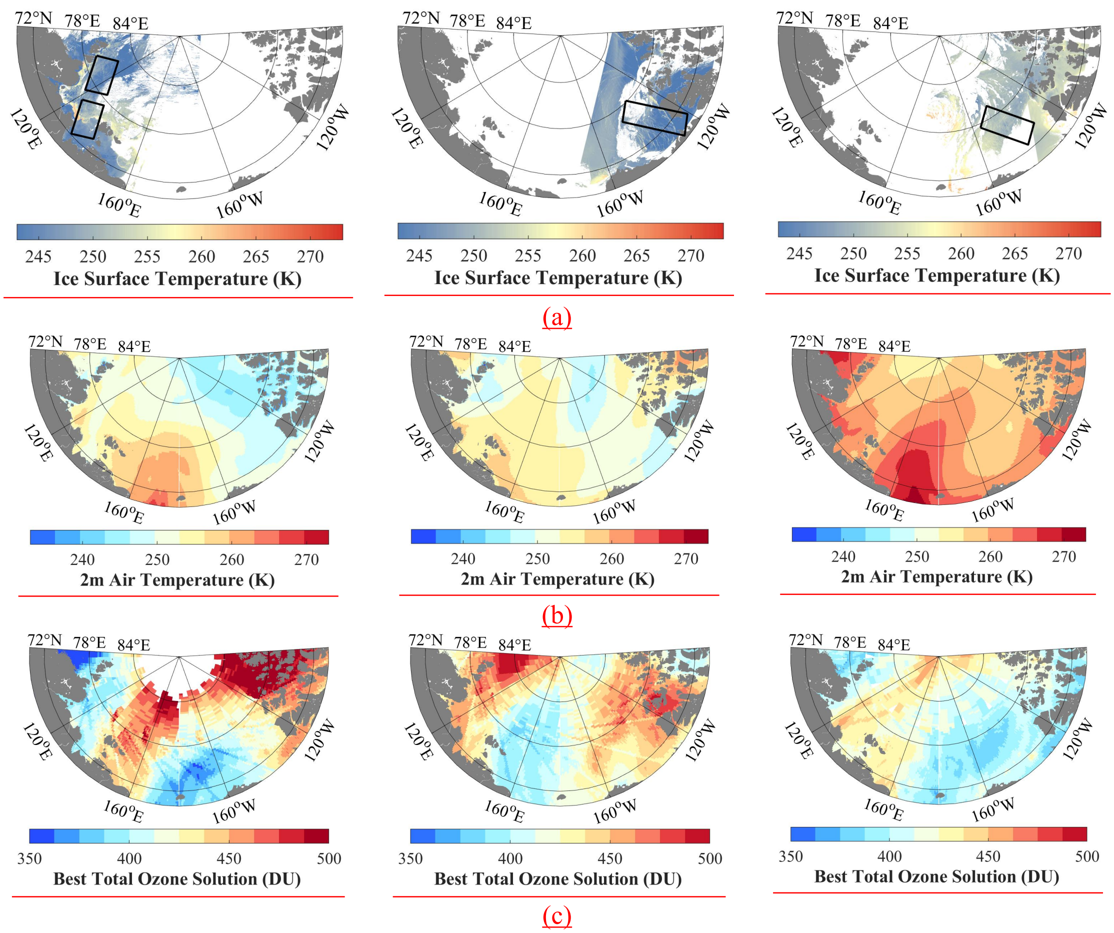

Figure 12: Temperature of ice surface and near-surface air and ozone solution for March 23, April 4, and 28, 2022 (columns left to right). (a) MODIS IST, where black borders indicate the TIS acquisition range on the day. (b) ERA5 2 m air temperature. (c) OMTO3 ozone solution.

First, as an important constraint on the Arctic lead detection, it is necessary to consider the impact of cloud interference. Although cloudy conditions are prevalent in the Arctic (see the large white area in the MODIS daily IST product shown in ~~Figure 12~~Fig. 12 (a)), due to the unavailable cloud products synchronised with the SDGSAT-1 TIS, this study only demonstrates the lead detection under clear sky conditions. However, we agree with the view of Hoffman et al. (2019) that using cloud mask products in ~~ice~~ leads detection would produce omissions as a result of incomplete cloud information. They reclassed the MODIS cloud mask products to eliminate omission errors and assumed that a lead pixel would have a BT less than 271 K (otherwise, it would be open water or warm cloud). We manually collected cloud-less data and used the BT filter, which rejected ~~the~~ pixels with BT values lower than approximately 245 K. Therefore, clouds are likely to ha~~ved~~ a relatively small impact on the results of this study, but the impact of warm clouds still remains. In the future, with the availability of the SDGSAT-1 cloud product, we can further investigate the lead detection for ~~the~~ cloudy conditions.

Apart from cloud interference, other atmospheric components also affect lead detection. The TIS B2 and B3 bands, the two atmospheric windows, are nearly transparent to the atmosphere, and therefore, to some extent, they can obtain surface radiance independent of the atmosphere. In contrast, the B1 band, as an absorption channel for ozone (Wan and Li, 1997), has attenuation in the atmosphere. As a result, the B1 band data present different temperature gradients from the other two bands, particularly pronounced at high latitudes (Prabhakara and Dalu, 1976). In addition, short-term temperature variations also affect the temperature contrast for the three thermal infrared bands and thus the detection of leads. Since the at-sensor BT data used in this study were not corrected for atmospheric radiation, this temperature variation results from a combination of sea ice radiation and atmospheric radiation. As displayed in ~~Figure 12~~Fig. 12, the temperature of sea ice surface and 2 m air, and the ozone ~~re~~solution present significant temporal and regional variations. Both the air and ice temperatures gradually increase and show similar spatial patterns. The ozone ~~re~~solution is high in the Laptev Sea and the Beaufort Sea, and its distribution changes rapidly on a monthly scale. We analyzed the sensitivity of lead temperature characteristics to these factors. First, based on the detected leads, we extracted the BT and BTA data only for those lead pixels and allocated them to ~~the~~ geographic grids at 30 km resolution (one tenth of the TIS swath width to allow comparison with coarse-resolution datasets). Then, regression analysis was conducted to find the relation between the thermal characteristics and IST, air temperature, or ozone ~~re~~solution, as listed in ~~the~~ Table 8.

In general, the BT data from the TIS three bands ~~have~~ show significant positive correlations with the IST ~~data~~ and air temperature. Although the upward slope of the BT data with respect to ice and air temperatures for the B1 band is smaller than that for B2 and B3 bands, the high correlation (~~of~~ 0.72 with the IST and 0.68 with the air temperature) demonstrates its effectiveness as a thermal infrared band for lead detection. On the other hand, changes in IST have only a small negative correlation with the BTA values of leads. While changes in air temperature are more likely to diminish the thermal contrast of ~~the~~ leads, which have less effect on the B1 band and more effect on the B2 band. These results imply that atmospheric correction and ice temperature retrieval of TIS thermal data could be effective approaches to improve the robustness of lead detection. Among ~~For~~ the three thermal infrared bands of the TIS, the B1 band may not be as sensitive to temperature variations as the B2 and B3 bands.

As we expected~~In our expectations~~, only the BT data from the B1 band exhibit ~~have~~ a negative correlation with ozone, with ~~the~~ a correlation of -0.62. This result is not surprising since~~Evidently,~~ only the B1 band radiance is heavily ~~strongly~~ absorbed by ozone, which also explains why the B1 band yields ~~gives~~ the lowest BT values for the presented cases in this ~~paper~~study. With respect to the BTA values of ~~the~~ leads, none of them show~~s~~ significant correlations with the ozone ~~re~~solution. This finding implies that although ozone affects the B1 band temperature measurement, it barely weakens the thermal contrast required for lead detection.

Table 8. Correlation between the thermal characteristics of SDGSAT-1 TIS three infrared bands and the IST, 2 m air temperature, and ozone ~~re~~solution, with the slope of the regression fitting in brackets.

	B1 band		**B2 band**		**B3 band**	
	BT value	BTA value	BT value	BTA value	BT value	BTA value
IST	**0.72**(0.49)	-0.26(-0.14)	**0.63**(0.63)	-0.40(-0.26)	**0.72**(0.59)	-0.37(-0.21)
Air temperature	**0.68** (0.53)	-0.39 (-0.26)	**0.68** (0.75)	-0.55 (-0.42)	**0.68** (0.63)	-0.50 (-0.25)
Ozone ~~re~~solution	**-0.62** (-0.07)	0.14 (-0.01)	-0.49 (-0.08)	0.19 (0.20)	-0.59 (-0.08)	0.24 (0.02)

5.2 Sea ice lead property resolved by the TIS

Due to thermal infrared imaging having long been limited to the moderate resolution of kilometers, it is difficult to confirm either the widths of narrow leads or the variations ~~inside~~ within them. The detection at the 30 m resolution allows for ~~presents~~ thermal variations to be observed ~~inside~~ within leads, as demonstrated in an interesting case shown ~~shown~~ in two row panels on the left of ~~Figure 13~~Fig. 13, which was acquired on April 3 over the Beaufort Sea. The TIS data present a noticeable transition zone (with a BTA value less than 2 K), which is likely seawater intrusion into the sea ice, while the lead in the center (with a BTA value greater than 3 K) was just opening. As the method ~~of~~ used in this study aims to extract all potential leads, the entire transition zone was marked as a~~n~~ ~~ice~~ lead. This is reasonable, as a previous study (Qu et al., 2020) used a BTA threshold of 1.2 K for potential leads, 1.5 K for general leads, and 2 K for open water discrimination. Given that the binary segmentation in this ~~paper~~ study applies a 1.8 K threshold, it again indicates that the thermal information obtained by SDGSAT-1 TIS presents a ~~greater~~ more significant thermal contrast.

Broadly speaking, fracture zones covered by thin ice and intruded by seawater are also considered as leads. For other supporting evidence, we incorporated the S1A SAR images acquired on the same day. ~~The dual-polarization data were radiometrically calibrated, and a false-color composition was performed by assigning the HH, the subtraction of HH by HV and the HV images to the red, green and blue channels, respectively.~~ The HH and HV SAR data ~~and~~ as well as the false-color composite images, are presented ~~shown~~ in the panel at the bottom right of ~~Figure 13~~Fig. 13. The overall backscatter values for the HH and HV data are low. However, in the transition zone of the lead, the backscatter values of the HH and HV data differ considerably, while ~~the~~ both the backscatter values are very low at the center opening~~opening in the center has low backscatter values~~. Accordingly, the transition zone presents ~~a~~ yellowish ~~color~~ in the false-color composite image, whereas ~~while~~ the opening lead is darker. Hence~~Therefore~~, the leads detected in this ~~paper~~ study based on thermal contrast are consistent with~~agree with~~ the properties resolved by the polarization differences in SAR. Regarding the application of SAR data to lead detection, its applicability to local sea ice conditions remains to be further explored.

In addition, contours of multiyear ice with high backscatter values ~~that are~~ observed in SAR images are similar to some negative BTA features. Such surface information is ~~In~~ particularly sensitive to the~~, the~~ B2 ~~band is more~~ band,~~sensitive to such surface information.~~ ~~This~~ suggest~~s~~ing surface temperature variations for different thicknesses of sea ice~~because various types of sea ice have different emissivity and produce different BT values~~. Similar surface temperature variations are also found in the 1 m resolution IST data obtained ~~derived~~ from helicopter-borne thermal infrared imaging (Thielke et al., 2022). Thanks to the high-resolution characterization of the SDGSAT-1 TIS and the accurate radiometric measurement, it is possible to reveal the sea ice properties, both ~~(~~inside the leads and on the ice surface~~)~~. However, ~~F~~for sea ice with a high-temperature characteristic, ~~(~~possibly due to thicker or local ~~resulting from local t~~temperature gradients~~)~~, its BTA can be ~~too~~ similar to that of a lead and can be difficult to ~~be~~ distinguish~~ed~~ (Key et al., 1993), which is why we preferred a BT filter after the lead segmentation in this study.

The special case shown in ~~Figure 10~~Fig. 10 (b) and (c) arouses our interest in understanding why the B2 ~~(b)~~ and B3 ~~(c)~~ bands missed some leads. As described in ~~Section~~ Sect. 4.2, the strip noise also affects lead detection. The strip noise is the most severe in the B3 band and secondary in the B2 band, while it is absent in the B1 band. This discrepancy ~~difference~~ arises ~~occurs~~ due to the fact that ~~because~~ when the TIS overpasses a homogeneous surface, which covers sea ice with a low radiance signal in this case, each detector generates ~~gives~~ a different noise bias (Corsini et al., 2000). This phenomenon is even more pronounced ~~severe~~ for detectors with higher signal-to-noise ratios. Likewise, to overcome the strip noise, it is necessary to apply the BT filter and use an appropriate threshold. In this case, t~~T~~he thresholds determined through ~~by~~ iterative selection were 243.93 K, 248.02 K and 247.14 K for B1, B2 and B3~~ in this case~~, respectively. Consequently, the high thresholds of B2 and B3 caused some lead details to be omitted during the detection process~~resulted in omissions of some lead details in the detection~~. From this perspective, residual noise in high-resolution thermal infrared images may have an impact on the lead detection based on the TIS B2 and B3 bands; whereas ~~while~~ the B1 band is less susceptible ~~affected~~ due to its relatively low sensitivity. It is noted that the forthcoming level-4b TIS data can suppress some of the stripe noise. On the other hand, as the TIS data available within the scope of this ~~paper~~ study is relatively limited, ~~these~~ the individual case studies presented may be weak in terms of generalizability. In the future, with support by a large amount of data, we aim to ~~will~~ develop ~~work on~~ a method that can overcome various ~~a variety of~~ interferences for application to SDGSAT-1 TIS data to more accurately detect sea ice leads.

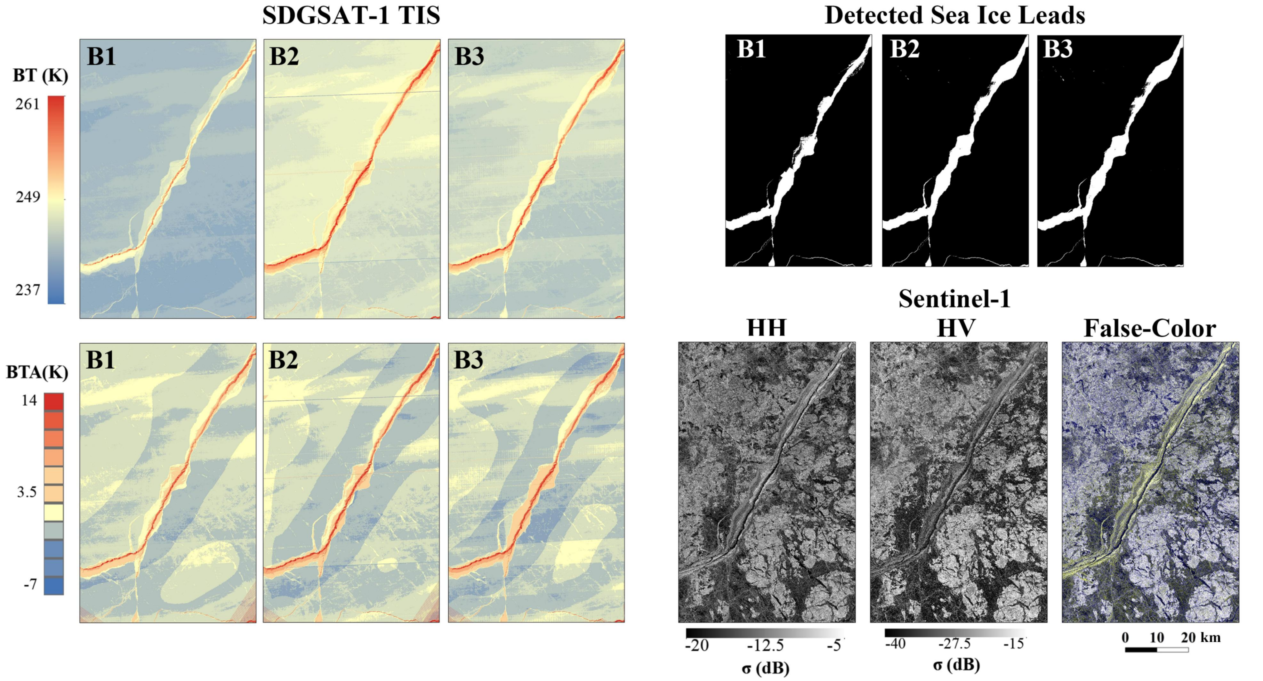

Figure 13: Comprehensive analysis for lead ~~properties~~ property in the Beaufort Sea based on SDGSAT-1 TIS data acquired at 04:28 UTC on April ~~28~~ 3 and the ~~derived leads, along with the~~ matched S1A data at 15:~~52~~ 53 UTC on the same day. Two parallel rows of panels on the left show the BT and BTA maps for the three bands of SDGSAT-1 TIS. The first row on the right panel shows the leads detected in this study. The panel at the bottom right displays the matched S1A HH, HV and false-color composite images ~~that present recognizable leads~~. SDGSAT-1 TIS data ID: KX10_TIS_20220403_W132.14_N74.67_202200033227.

6 Summary and conclusion

Over the past decades, the Arctic has experienced increasing temperatures and a rapid retreat of sea ice~~the increasing Arctic temperatures and rapid retreat of sea ice~~, ~~include have~~with profound implications for both the Arctic and the extra-polar climate and ecosystems. Sea ice leads play a critical role in regulating~~are a key factor influencing~~ the heat exchange between the ocean and the overlying atmosphere. However, previous lead observations based on thermal infrared remote sensing have long been limited to moderate resolutions on a kilometer scale, making it challenging to resolve lead details and resulting in inadequate estimates for ~~ice~~ lead parameters. There is an urgent need to develop fine-scale dataset~~s~~ of sea ice leads.

The recently launched SDGSAT-1 provides an emerging opportunity to detect leads at high spatial resolutions up to 30 m by its onboard ~~payload the~~ TIS payload. This ~~paper~~ study demonstrates the feasibility of using the three TIS infrared bands for detecting ~~ice~~ leads in the Arctic Ocean. We proposed a method that combines binary segmentation with the BT filter to detect leads by the three TIS ~~data in three~~ bands. The detection results show great details ~~of~~ on ~~the~~ narrow leads of tens of meters in width, as well as high accuracy. For example, in the Beaufort Sea case in April 2022, the overall accuracies are 96.24%, 96.34% and 96.3~~3~~% for the B1, B2 and B3 bands, respectively, compared with the S2 visible images at 10 m resolution. ~~Because~~ Since more narrow leads are detected by the TIS, the TIS-derived lead areas are 1.3 times more than the results based on the MODIS IST data at a 1 km resolution in the 11 collected cases. ~~This~~ Our finding indicates that more leads exist in the Arctic Ocean than we have ever observed. These narrow leads beyond our expectations would allow for more heat exchange (Marcq and Weiss, 2012). Therefore, the TIS sensor is expected to improve the lead representation, which is crucial for climate models.

The cross-comparisons among the TIS three infrared bands suggest that the B2 and B3 bands have similar performances in detecting leads, whereas the B2 band yields the best performance among the three bands. Although the B1 band is less commonly used in thermal infrared measurements, the leads detected by the B1 band can be complementary to the other two on some occasions. We therefore recommend ~~suggest~~ using the combined results of the leads detected from the three TIS bands.

Furthermore, the analysis of the correlation between the detected leads and temperature suggests that the B1 (both its BT and BTA data) is ~~not~~ less sensitive to the variations in surface and near-surface temperature. Although ozone in the atmosphere absorbs B1 band radiance, ozone has little impact on the lead detection ~~of ice leads~~ by the B1 band. The different sensitivity of the B1 band to surface information and atmospheric conditions from the other two bands produces an unexpected performance in sea ice lead detection. Regarding the variations inside the leads, an analysis incorporating the S1A data agrees with the lead properties revealed by our results, but the threshold currently used does classify the transition zone as ~~an~~ a ~~ice~~ lead. Thanks to the sufficiently high resolution of the SDGSAT-1 TIS, it is expected to provide crucial data for the analysis of lead formation and refreezing based on sequential thermal infrared data, an aspect that deserves future attention.

This study ~~is the first to~~ investigates the detection of sea ice leads by spaceborne thermal infrared remote sensing at a high spatial resolution of tens of meters. The results demonstrate that the TIS onboard SDGAST-1 has excellent potential for detecting sea ice leads (as well as possible IST retrieval) in polar regions. Nevertheless, limited by the imaging time and cloudy conditions over the Arctic region, only individual case studies based on TIS data were carried out. Along with the acquisition of more TIS data~~more TIS data acquired in the Arctic~~ throughout an entire year and the development of near-real-time cloud product, we can expect to investigate its capability for the lead detection ~~of ice leads~~ in different seasons. ~~By c~~Combining this data with ~~more~~ diverse datasets of sea ice, we ~~wish~~ aim to provide insights into the contribution of leads to Arctic sea ice dynamics in an effort to support SDG 13: climate action.

Furthermore, our investigation suggests that the TIS has high sensitivity to surface temperature changes, yielding great temperature contrasts to distinguish anomalies. The three infrared bands of the TIS present different sensitivities, thus allowing surface radiation detection and underpinning the surface temperature retrieval applying three thermal infrared bands. Encouragingly, the sensor should also have great potentials on supporting research related to other SDG indicators.~~,~~ F~~f~~or instance, it could aid ~~SDG 7~~ in investigating the urban heat island effect to promote green cities,~~;~~ monitoring wildfire and heatwave events to understand impacts of climate change (SDG 13), and ~~SDG 14 in~~ monitoring industrial ~~wastewater~~ discharges in coastal zone to protect marine ecosystem (SDG 14)~~, and SDG 13 for monitoring wildfire and heatwave events to understand impacts of climate change~~. The TIS, together with the other two sensors onboard SDGSAT-1, ~~are~~ is expected to provide ~~more~~ valuable data to facilitate a global approach to the SDGs.

Data availability

The SDGSAT-1 TIS data can be acquired from the International Research Center of Big Data for Substantial Development Goals (www.sdgsat.ac.cn/, last access: 20 December 2022). The S2 data are available on the United States Geological Survey website (https://www.usgs.gov/, last access: 20 December 2022). The S1 data are accessed from the Copernicus Open Access Hub (https://scihub.copernicus.eu/dhus/#/home/, last access: 20 December 2022). The MOD29~~P1D~~ product can be acquired from the National Snow and Ice Data Center (https://nsidc.org/, last access: ~~20~~ 1 ~~December~~ March ~~2022~~2023; Hall and Riggs, 2021). The ERA5 datasets are available on European Centre for Medium-Range Weather Forecasts (https://cds.climate.copernicus.eu/, last access: 20 December 2022; Hersbach et al., 2018). The OMTO3 products can be acquired from the NASA Earth Observation Data web (https://disc.gsfc.nasa.gov/, last access: 20 December 2022; Bhartia, 2012). The sea ice lead dataset published by Hoffman et al. (2022b) are available from https://doi.org/10.5061/dryad.79cnp5hz2 (last access: 20 December 2022).

Author contribution

XML conceived the idea and designed the research. YQ developed the method and conducted the experiments. HDG provided insightful suggestions and discussions. All authors contributed to writing the manuscript.

Competing interests

The authors declare that no conflicts of interest or personal relationships influenced the work reported in this paper.

Acknowledgements

It is acknowledged that the SDGSAT-1 data are provided by the International Research Center of Big Data for Substantial Development Goals, and other data used is also acknowledged. The authors particularly thank the team led by Dr. Hongyu Chen and Bihong Fu in Innovation Academy of Microsatellites of CAS and the team led by Dr. Fansheng Chen in Shanghai Institute of Technical Physics of CAS for their great efforts on development of the SDGSAT-1 satellite and the onboard TIS payload. Mr. Weixing Wang from the SDGSAT-1 ground segment team of Aerospace Information Research Institute of CAS provides great support on the TIS data acquisitions over the Arctic. Dr. Yonghong Hu from the SDGSAT-1 calibration team of AIR, CAS explained the calibration of the TIS data.

Funding

The study is partially supported by the National Science Fund for Distinguished Young Scholars (No. 42025605).

References

Ackerman, S. A., Strabala, K. I., Menzel, W. P., Frey, R. A., Moeller, C. C., and Gumley, L. E.: Discriminating clear sky from clouds with MODIS, Journal of Geophysical Research: Atmospheres, 103, 32141-32157, 10.1029/1998JD200032, 1998.

Alam, A. and Curry, J. A.: Evolution of new ice and turbulent fluxes over freezing winter leads, Journal of Geophysical Research: Oceans, 103, 15783-15802, 10.1029/98JC01188, 1998.

Alvarez, A.: A model for the Artic mixed layer circulation under a melted lead: Implications on the near-surface temperature maximum formation, The Cryosphere Discussions, 1-14, 10.5194/tc-2022-233, 2020.

~~Arrhenius, S.: XXXI. On the influence of carbonic acid in the air upon the temperature of the ground, The London, Edinburgh, and Dublin Philosophical Magazine and Journal of Science, 41, 237-276, 10.1080/14786449608620846, 1896.~~

Bhartia, P. K.: OMI/Aura TOMS-Like Ozone and Radiative Cloud Fraction L3 1 day 0.25 degree x 0.25 degree V3 [dataset], https://doi.org/10.5067/Aura/OMI/DATA3002, 2012.

Bhartia, P. K.: OMI Algorithm Theoretical Basis Document, Volume II, OMI Ozone Products, Greenbelt, Maryland, USA, NASA Goddard Space Flight Center, 2002.

Bröhan, D. and Kaleschke, L.: A nine-year climatology of Arctic sea ice lead orientation and frequency from AMSR-E, Remote Sensing, 6, 1451-1475, 10.3390/rs6021451, 2014.

Cavalieri, D. J. and Parkinson, C. L.: Arctic sea ice variability and trends, 1979 – 2010, The Cryosphere, 6, 881-889, 10.5194/tc-6-881-2012, 2012.

Corsini, G., Diani, M., and Walzel, T.: Striping removal in MOS-B data, IEEE Transactions on Geoscience and Remote Sensing, 38, 1439-1446, 10.1109/36.843038, 2000.

Eurpean Space Agency (ESA): Sentinel-1 User Handbook, 2013.

Eurpean Space Agency (ESA): Sentinel-2 User Handbook, 2015.

Fan, P., Pang, X., Zhao, X., Shokr, M., Lei, R., Qu, M., Ji, Q., and Ding, M.: Sea ice surface temperature retrieval from Landsat 8/TIRS: Evaluation of five methods against in situ temperature records and MODIS IST in Arctic region, Remote Sensing of Environment, 248, 111975, 10.1016/j.rse.2020.111975, 2020.

Gimbert, F., Jourdain, N. C., Marsan, D., Weiss, J., and Barnier, B.: Recent mechanical weakening of the Arctic sea ice cover as revealed from larger inertial oscillations, Journal of Geophysical Research: Oceans, 117, 10.1029/2011JC007633, 2012.

Guo, H.: From Digital Earth to big Earth data: accelerating scientific discovery and supporting global sustainable development, International Journal of Digital Earth, 12, 1-1, 10.1080/17538947.2018.1559481, 2019.

Guo, H., Liang, D., Chen, F., and Shirazi, Z.: Innovative approaches to the Sustainable Development Goals using Big Earth Data, Big Earth Data, 5, 263-276, 10.1080/20964471.2021.1939989, 2021.

Guo, H. D., Changyong; Chen, Hongyu; Liu, Jianbo; Fu, Bihong; Li, Xiaoming; Zou, Ziming; Liang, Dong;: SDGSAT-1: The World's First Scientific Satellite for Sustainable Development Goals, Science Bulletin, 2022.

~~Guo, H., Liang, D., Chen, F., and Shirazi, Z.: Innovative approaches to the Sustainable Development Goals using Big Earth Data, Big Earth Data, 5, 263-276, 10.1080/20964471.2021.1939989, 2021.~~

~~Hall, D. K. and Riggs, G. A.: MODIS/Terra Sea Ice Extent Daily L3 Global 1km EASE-Grid Day, Version 61 [dataset], https://doi.org/10.5067/MODIS/MOD29P1D.061, 2021.~~

Hall, D. K. and Riggs., G.: MODIS/Terra Sea Ice Extent 5-Min L2 Swath 1km, Version 61 [dataset], https://doi.org/10.5067/MODIS/MOD29.061, 2021.

Hall, D. K., Riggs, G. A., Salomonson, V. V., Barton, J., Casey, K., Chien, J., DiGirolamo, N., Klein, A., Powell, H., and Tait, A.: Algorithm theoretical basis document (ATBD) for the MODIS snow and sea ice-mapping algorithms, Nasa Gsfc, 45, 2001.

Hall, D. K., Key, J. R., Casey, K. A., Riggs, G. A., and Cavalieri, D. J.: Sea ice surface temperature product from MODIS, IEEE transactions on geoscience and remote sensing, 42, 1076-1087, 10.1109/TGRS.2004.825587, 2004.

~~Hall, D. K., Riggs, G. A., Salomonson, V. V., Barton, J., Casey, K., Chien, J., DiGirolamo, N., Klein, A., Powell, H., and Tait, A.: Algorithm theoretical basis document (ATBD) for the MODIS snow and sea ice-mapping algorithms, Nasa Gsfc, 45, 2001.~~

Hersbach, H., Bell, B., Berrisford, P., Biavati, G., Horányi, A., Muñoz Sabater, J., Nicolas, J., Peubey, C., Radu, R., Rozum, I., Schepers, D., Simmons, A., Soci, C., Dee, D., and Thépaut, J.-N.: ERA5 hourly data on single levels from 1959 to present [dataset], https://doi.org/10.24381/cds.adbb2d47, 2018.

Hoffman, J. P., Ackerman, S. A., Liu, Y., and Key, J. R.: The detection and characterization of Arctic Sea ice leads with satellite imagers, Remote Sensing, 11, 521, 10.3390/rs11050521 2019.

Hoffman, J. P., Ackerman, S. A., Liu, Y., Key, J. R., and McConnell, I. L.: Application of a convolutional neural network for the detection of sea ice leads, Remote Sensing, 13, 4571, 10.3390/rs13224571, 2021.

Hoffman, J. P., Ackerman, S. A., Liu, Y., and Key, J. R.: A 20-Year Climatology of Sea Ice Leads Detected in Infrared Satellite Imagery Using a Convolutional Neural Network, Remote Sensing, 14, 5763, 10.3390/rs14225763, 2022a.

Hoffman, J., Ackerman, S., Liu, Y., Key, J., and McConnell, I.: MODIS Sea ice leads detections using a U-Net [dataset], https://doi.org/10.5061/dryad.79cnp5hz2, 2022b.

~~Hoffman, J. P., Ackerman, S. A., Liu, Y., Key, J. R., and McConnell, I. L.: Application of a convolutional neural network for the detection of sea ice leads, Remote Sensing, 13, 4571, 10.3390/rs13224571, 2021.~~

Hu, Y., Li, X.-M., Dou, C., Chen, F., Jia, G., Hu, Z., Xu, A., Ren, Y., Yan, L., Wang, N., and Cui, Z.: Absolute radiometric calibration evaluation for Thermal Infrared Spectrometer (TIS) onboard SDGSAT-1 satellite [Unpublished manuscript], 2022.

Hu, Z., Zhu, M., Wang, Q., Su, X., and Chen, F.: SDGSAT-1 TIS Prelaunch Radiometric Calibration and Performance, Remote Sensing, 14, 4543, 10.3390/rs14184543, 2022.

International Research Center of Big Data for Sustainable Development Goals (CBAS): SDGSAT-1 Data Users Handbook (Draft), 2022. http://60.245.209.56/preview/20221125/c84c0b5d89984cd384ffa05dbb163d14.pdf

Key, J., Stone, R., Maslanik, J., and Ellefsen, E.: The detectability of sea-ice leads in satellite data as a function of atmospheric conditions and measurement scale, Annals of Glaciology, 17, 227-232, 10.3189/S026030550001288X, 1993.

Key, J., Maslanik, J., and Ellefsen, E.: The effects of sensor field-of-view on the geometrical characteristics of sea ice leads and implications for large-area heat flux estimates, Remote sensing of environment, 48, 347-357, 10.1016/0034-4257(94)90009-4, 1994.

Key, J. R., Collins, J. B., Fowler, C., and Stone, R. S.: High-latitude surface temperature estimates from thermal satellite data, Remote Sensing of Environment, 61, 302-309, 10.1016/S0034-4257(97)89497-7, 1997.

~~König, M., Hieronymi, M., and Oppelt, N.: Application of sentinel-2 MSI in Arctic research: Evaluating the performance of atmospheric correction approaches over Arctic sea ice, Frontiers in Earth Science, 7, 22, 10.3389/feart.2019.00022, 2019.~~

Kwok, R.: Arctic sea ice thickness, volume, and multiyear ice coverage: losses and coupled variability (1958 – 2018), Environmental Research Letters, 13, 105005, 10.1088/1748-9326/aae3ec, 2018.

Ledley, T. S.: A coupled energy balance climate - sea ice model: Impact of sea ice and leads on climate, Journal of Geophysical Research: Atmospheres, 93, 15919-15932, 10.1029/JD093iD12p15919, 1988.

Lee, S., Kim, H.-c., and Im, J.: Arctic lead detection using a waveform mixture algorithm from CryoSat-2 data, The Cryosphere, 12, 1665-1679, 10.5194/tc-12-1665-2018, 2018.

Liang, Z., Pang, X., Ji, Q., Zhao, X., Li, G., and Chen, Y.: An Entropy-Weighted Network for Polar Sea Ice Open Lead Detection From Sentinel-1 SAR Images, IEEE Transactions on Geoscience and Remote Sensing, 60, 1-14, 10.1109/TGRS.2022.3169892, 2022.

Lindsay, R. and Rothrock, D.: Arctic sea ice leads from advanced very high resolution radiometer images, Journal of Geophysical Research: Oceans, 100, 4533-4544, 10.1029/94JC02393, 1995.

Liu, W., Li, J., Zhang, Y., Zhao, L., and Cheng, Q.: Preflight radiometric calibration of TIS sensor onboard SDG-1 satellite and estimation of its LST retrieval ability, Remote sensing, 13, 3242, 10.3390/rs13163242, 2021.

Lüpkes, C., Vihma, T., Birnbaum, G., and Wacker, U.: Influence of leads in sea ice on the temperature of the atmospheric boundary layer during polar night, Geophysical Research Letters, 35, 10.1029/2007GL032461, 2008.

Marcq, S. and Weiss, J.: Influence of sea ice lead-width distribution on turbulent heat transfer between the ocean and the atmosphere, The Cryosphere, 6, 143-156, 10.5194/tc-6-143-2012, 2012.

Maykut, G. A.: Large-scale heat exchange and ice production in the central Arctic, Journal of Geophysical Research: Oceans, 87, 7971-7984, 10.1029/JC087iC10p07971, 1982.

McIntire, T. J. and Simpson, J. J.: Arctic sea ice, cloud, water, and lead classification using neural networks and 1.6-/spl mu/m data, IEEE Transactions on Geoscience and Remote Sensing, 40, 1956-1972, 10.1109/TGRS.2002.803728, 2002.

MODIS Characterization Support Team: MODIS Geolocation Fields Product [dataset], http://dx.doi.org/10.5067/MODIS/MOD03.061, 2017.

Muchow, M., Schmitt, A. U., and Kaleschke, L.: A lead-width distribution for Antarctic sea ice: a case study for the Weddell Sea with high-resolution Sentinel-2 images, The Cryosphere, 15, 4527-4537, 10.5194/tc-15-4527-2021, 2021.

Murashkin, D., Spreen, G., Huntemann, M., and Dierking, W.: Method for detection of leads from Sentinel-1 SAR images, Annals of Glaciology, 59, 124-136, 10.1017/aog.2018.6, 2018.

Murashkin, D. and Spreen, G.: Sea ice leads detected from sentinel-1 SAR images, IGARSS 2019 IEEE International Geoscience and Remote Sensing Symposium, 174-177,— 10.1109/IGARSS.2019.8898043,

Ólason, E., Rampal, P., and Dansereau, V.: On the statistical properties of sea-ice lead fraction and heat fluxes in the Arctic, The Cryosphere, 15, 1053-1064, 10.5194/tc-15-1053-2021, 2021.

Onarheim, I. H., Eldevik, T., Smedsrud, L. H., and Stroeve, J. C.: Seasonal and regional manifestation of Arctic sea ice loss, Journal of Climate, 31, 4917-4932, 10.1175/JCLI-D-17-0427.1, 2018.

Otsu, N.: A threshold selection method from gray-level histograms, IEEE transactions on systems, man, and cybernetics, 9, 62-66, 10.1109/TSMC.1979.4310076, 1979.

Prabhakara, C. and Dalu, G.: Remote sensing of the surface emissivity at 9 µm over the globe, Journal of Geophysical Research, 81, 3719-3724, 10.1029/JC081I021P03719, 1976.

Qu, M., Pang, X., Zhao, X., Zhang, J., Ji, Q., and Fan, P.: Estimation of turbulent heat flux over leads using satellite thermal images, The Cryosphere, 13, 1565-1582, 10.5194/tc-13-1565-2019, 2019.

Qu, M., Pang, X., Zhao, X., Lei, R., Ji, Q., Liu, Y., and Chen, Y.: Spring leads in the Beaufort Sea and its interannual trend using Terra/MODIS thermal imagery, Remote Sensing of Environment, 256, 112342, 10.1016/j.rse.2021.112342, 2021.

Rampal, P., Weiss, J., and Marsan, D.: Positive trend in the mean speed and deformation rate of Arctic sea ice, 1979–2007, Journal of Geophysical Research: Oceans, 114, 10.1029/2008JC005066, 2009.

Reiser, F., Willmes, S., and Heinemann, G.: A new algorithm for daily sea ice lead identification in the Arctic and Antarctic winter from thermal-infrared satellite imagery, Remote Sensing, 12, 1957, 10.3390/rs12121957 2020.

Ridler, T. and Calvard, S.: Picture thresholding using an iterative selection method, IEEE trans syst Man Cybern, 8, 630-632, 10.1109/TSMC.1978.4310039, 1978.

Röhrs, J. and Kaleschke, L.: An algorithm to detect sea ice leads by using AMSR-E passive microwave imagery, The Cryosphere, 6, 343-352, 10.5194/tc-6-343-2012, 2012.

Serreze, M. C. and Francis, J. A: The Arctic amplification debate. Climatic Change, 76, 241–264, 10.1007/s10584-005-9017-y, 2006

Serreze, M. C. and Barry, R. G.: Processes and impacts of Arctic amplification: A research synthesis, Global and planetary change, 77, 85-96, 10.1016/j.gloplacha.2011.03.004, 2011.

Steele, M., Dickinson, S., Zhang, J., and W. Lindsay, R.: Seasonal ice loss in the Beaufort Sea: Toward synchrony and prediction, Journal of Geophysical Research: Oceans, 120, 1118-1132, 10.1002/2014JC010247, 2015.

Stroeve, J. C., Serreze, M. C., Holland, M. M., Kay, J. E., Malanik, J., and Barrett, A. P.: The Arctic's rapidly shrinking sea ice cover: a research synthesis, Climatic change, 110, 1005-1027, 10.1007/s10584-011-0101-1, 2012.

Thielke, L., Huntemann, M., Hendricks, S., Jutila, A., Ricker, R., and Spreen, G.: Sea ice surface temperatures from helicopter-borne thermal infrared imaging during the MOSAiC expedition, Scientific Data, 9, 364, 10.1038/s41597-022-01461-9, 2022.

Tschudi, M., Curry, J., and Maslanik, J.: Characterization of springtime leads in the Beaufort/Chukchi Seas from airborne and satellite observations during FIRE/SHEBA, Journal of Geophysical Research: Oceans, 107, SHE 9-1-SHE 9-14, 10.1029/2000JC000541, 2002.

Vihma, T., Pirazzini, R., Fer, I., Renfrew, I. A., Sedlar, J., Tjernström, M., Lüpkes, C., Nygård, T., Notz, D., and Weiss, J.: Advances in understanding and parameterization of small-scale physical processes in the marine Arctic climate system: a review, Atmospheric Chemistry and Physics, 14, 9403-9450, 10.5194/acp-14-9403-2014, 2014.

Wan, Z. and Li, Z.-L.: A physics-based algorithm for retrieving land-surface emissivity and temperature from EOS/MODIS data, IEEE Transactions on Geoscience and Remote Sensing, 35, 980-996, 10.1109/36.602541, 1997.

Wang, Q., Shokr, M., Chen, S., Zheng, Z., Cheng, X., and Hui, F.: Winter Sea-Ice Lead Detection in Arctic Using FY-3D MERSI-II Data, IEEE Geoscience and Remote Sensing Letters, 19, 1-5, 10.1109/LGRS.2022.3223689, 2022.

Wernecke, A. and Kaleschke, L.: Lead detection in Arctic sea ice from CryoSat-2: quality assessment, lead area fraction and width distribution, The Cryosphere, 9, 1955-1968, 10.5194/tc-9-1955-2015, 2015.

Willmes, S. and Heinemann, G.: Pan-Arctic lead detection from MODIS thermal infrared imagery, Annals of Glaciology, 56, 29-37, 10.3189/2015AoG69A615, 2015a.

Willmes, S. and Heinemann, G.: Sea-ice wintertime lead frequencies and regional characteristics in the Arctic, 2003–2015, Remote Sensing, 8, 4, 10.3390/rs8010004 2015b.

~~Willmes, S. and Heinemann, G.: Daily pan-arctic sea-ice lead maps for 2003–2015, with links to maps in netCDF format, Supplement to: Willmes, S; Heinemann, G, 2003-2015, 10.1594/PANGAEA.854411, 2015.~~

Yin, Z., Li, X., Ge, Y., Shang, C., Li, X., Du, Y., and Ling, F.: Estimating subpixel turbulent heat flux over leads from MODIS thermal infrared imagery with deep learning, The Cryosphere, 15, 2835-2856, 10.5194/tc-15-2835-2021, 2021.

Zhang, Y., Cheng, X., Liu, J., and Hui, F.: The potential of sea ice leads as a predictor for summer Arctic sea ice extent, The Cryosphere, 12, 3747-3757, 10.5194/tc-12-3747-2018, 2018.

Zhong, W., Jiang, M., Xu, K., and Jia, Y.: Arctic Sea Ice Lead Detection from Chinese HY-2B Radar Altimeter Data, Remote Sensing, 15, 516, 10.3390/rs15020516, 2023.